ELSEVIER

Marine Geology 240 (2007) 19–41

MARINE GEOLOGY
INTERNATIONAL JOURNAL OF MARINE GEOLOGY, GEOCHEMISTRY AND GEOPHYSICS

www.elsevier.com/locate/margeo

Origin of continental margin morphology: Submarine-slide or downslope current-controlled bedforms, a rock magnetic approach

K. Schwehr *, N. Driscoll, L. Tauxe

Scripps Institution of Oceanography, University of California San Diego, San Diego, CA 92093-2002, USA

Received 24 March 2006; received in revised form 24 January 2007; accepted 31 January 2007

Abstract

Morphological features observed in both swath bathymetry and seismic reflection data are not unique, which introduces uncertainty as to their origin. The origin of features observed in the Humboldt Slide has generated much controversy because the same features have been interpreted as a submarine failure deposit versus current-controlled sediment waves. It is important to resolve this controversy because similar structures are observed on many continental margins and the origin of these features needs to be understood. Anisotropy of magnetic susceptibility (AMS) measurements on sediment samples acquired from the Humboldt Slide reveal that the top ~ 8 m have not experienced post-depositional deformation. This suggests that these features are formed by primary deposition associated with downslope currents. Using the same AMS technique on a core acquired north of the Humboldt Slide in a region with no geophysical evidence for post-depositional deformation, we were able to identify a ~ 1 m thick deposit that appears to be a small slump.

Keywords: submarine landslides; slope failure; anisotropy of magnetic susceptibility; STRATAFORM; Humboldt Slide; Eel River Basin

1. Introduction

Geologists have long appreciated the importance of submarine landslides and failures in the development of unconformities (Embley and Jacobi, 1986; Booth et al., 1993; Evans et al., 1996). Recently there has been much debate concerning the identification of submarine landslides and rotational slumps in seismic reflection data (Dillon et al., 1993; Gardner et al., 1999; Holbrook, 2001; Holbrook et al., 2002; Lee et al., 2002; Trincardi et al., 2004). The controversy arises, in large part, because the stratal geometry of many deposits, previously identified as retrogressive slumps, is not unique and could equally be generated from down- or along-slope currents (e.g. Blake–Bahama collapse structure, Holbrook et al., 2002; Humboldt Slide in the Eel River Basin, Fig. 1).

Deposition and erosion of the slope may be caused by a number of different processes (e.g., slope failure, incision and overbank deposits, bottom currents, shelf-edge deltas). Understanding how these processes sculpt the continental slope is critical to generating quantitative geologic models of continental slope evolution (Pratson and Coakley, 1996; Driscoll and Diebold, 1999). Developing a test to discriminate between these alternative scenarios, retrogressive slumps versus current-controlled deposits, would provide valuable new insights into the origin of these deposits and their relative importance in the construction and evolution of continental margins.

* Corresponding author.
E-mail address: kurt@ccom.unh.edu (K. Schwehr).

0025-3227/$ - see front matter © 2007 Elsevier B.V. All rights reserved.
doi:10.1016/j.margeo.2007.01.012

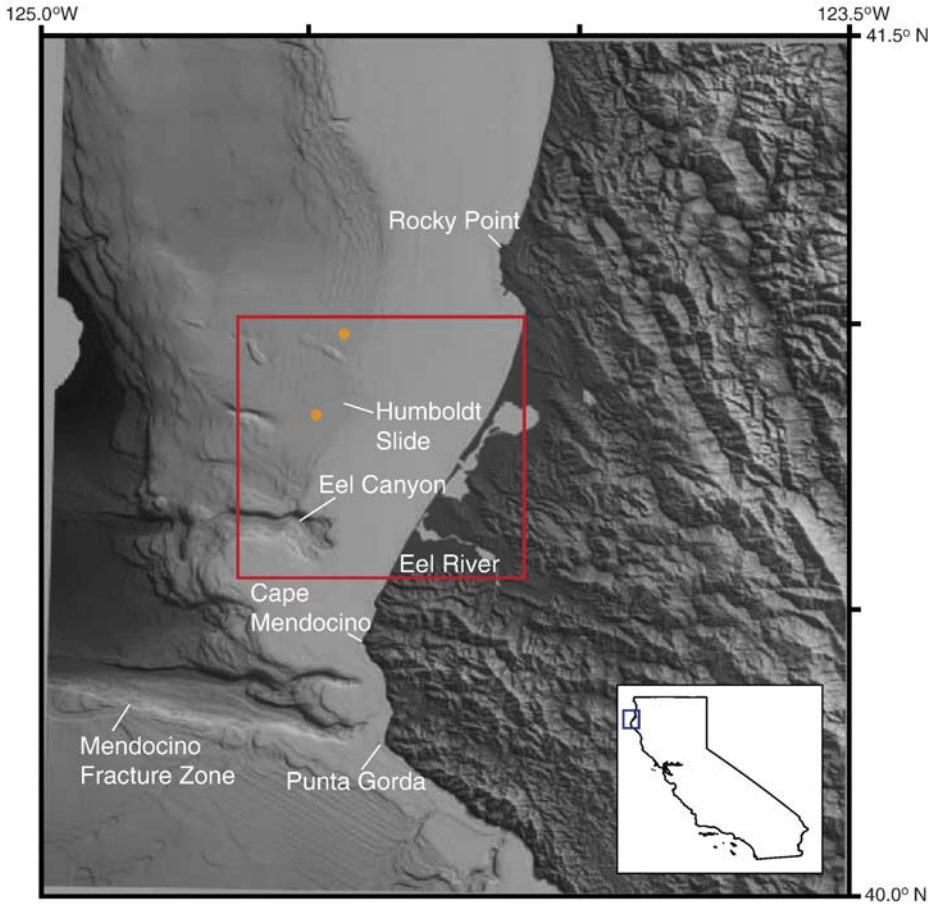

Fig. 1. The Eel River Basin is located in northern California, just north of the Mendocino Triple Junction. The Eel River enters the ocean south of Humboldt Bay. The slide is bounded by the Little Salmon Fault Zone to the north, the Eel Canyon to the south and up dip is delineated by the shelf break. The bathymetry is a compilation of the STRATAFORM EM1000, MBARI EM300 and the NOAA coastal relief 3 second data. The red box shows the location of the study area (Fig. 2) with the core locations marked with orange circles.

Gardner et al. (1999) interpreted the Humboldt Slide as having been formed by retrogressive failure and rotation of blocks above a shear zone. Lee et al. (2002) reinterpreted the Humboldt Slide complex as sediment waves emplaced by downslope gravity flows and argued that sediment waves are infilling a slide scar. The differing interpretations of the structure by Gardner et al. (1999) and Lee et al. (2002) highlight the ongoing controversy regarding the origin of this type of morphological feature around the globe (of which the Humboldt Slide complex is only one such example). These two interpretations (primary depositional features versus retrogressive faulting and internal deformation) are based on the same Huntec (Dodds, 1980) seismic data set.

The difficulties of interpreting such structures are illustrated by the Blake–Bahama outer ridge. Holbrook (2001) reinterpreted existing USGS data from the Blake–Bahama outer ridge and refined the previous interpretation of Dillon et al. (1993) that the observed features were normal faults associated with a gas-hydrate collapse structure. By examining the stratal geometry, Holbrook (2001) suggested the structures were growth faults recording several events, not just one event as suggested by Dillon et al. (1993). Subsequently, Holbrook et al. (2002) conducted an expensive 3D seismic survey to define the nature of the collapse structures. After acquiring the seismic data set, Holbrook et al. (2002) concluded that the features were in fact not growth faults, but were actually sediment waves.

In this paper, we apply a test based on sedimentary fabric as characterized by anisotropy of magnetic susceptibility (AMS) for assessing the origin of these ambiguous features of the Humboldt Slide. The test is based on magnetic fabrics to determine the extent of post-depositional deformation, a prediction of the retrogressive failure hypothesis. We will outline and describe the results.

2. Geologic setting

The ongoing deformation, uplift, and erosion of the Californian hinterland provide vast amounts of sediment to the U.S. Pacific continental margin (Clarke, 1987; Field and Barber, 1993). The relatively high rate of sedimentation and recurrence of earthquakes (Couch, 1980) makes the Eel River Basin an ideal locale to examine slope failure and consequent slide deposits. In addition to strong forcing functions, vast amounts of data have been acquired in the Eel Basin as part of the ONR STRATAFORM project (Nittrouer, 1999). This background allows us to place our results into a well-defined geological framework.

The Humboldt Slide deposit mantles a bowl-shaped depression that extends from the outer shelf to the middle slope on the Eel Margin (Fig. 2). On the basis of the internal geometry and surficial morphology of the Humboldt Slide deposit, two competing hypotheses have emerged: (1) The Humboldt Slide deposit and internal geometry were formed by retrogressive failure and rotation above a shear zone (detachment) with minimal lateral translation of the deformed sediment carapace (Gardner et al., 1999), and (2) The deposit records primary deposition by density currents (hyperpycnal flows) cascading down a pre-existing slide scar (Lee et al., 2002). In the primary deposition scenario, previous slope failure and evacuation of the failed material over-steepened the local slope and created the Humboldt Slide scar. Acceleration of the density flows in response to the locally over-steepened slope gives rise to current-controlled bedforms in this region.

The Eel River Basin has a narrow shelf (22 km from the Eel River to the shelf break above the Humboldt Slide) such that sediment can potentially escape over the shelf break onto the shelf slope and beyond (Alexander and Simoneau, 1999). The typical winter swell can re-suspend sand in 50–80 m of water, whereas large storms can rework sand on the middle to outer shelf, and perhaps down to the upper slope (Alexander and Simoneau, 1999). Deposition rates derived from ^{210}Pb and ^{137}Cs reveal high sediment accumulation rates (SAR) on the shelf, and on the slope in the area of the Humboldt Slide (Alexander and Simoneau, 1999).

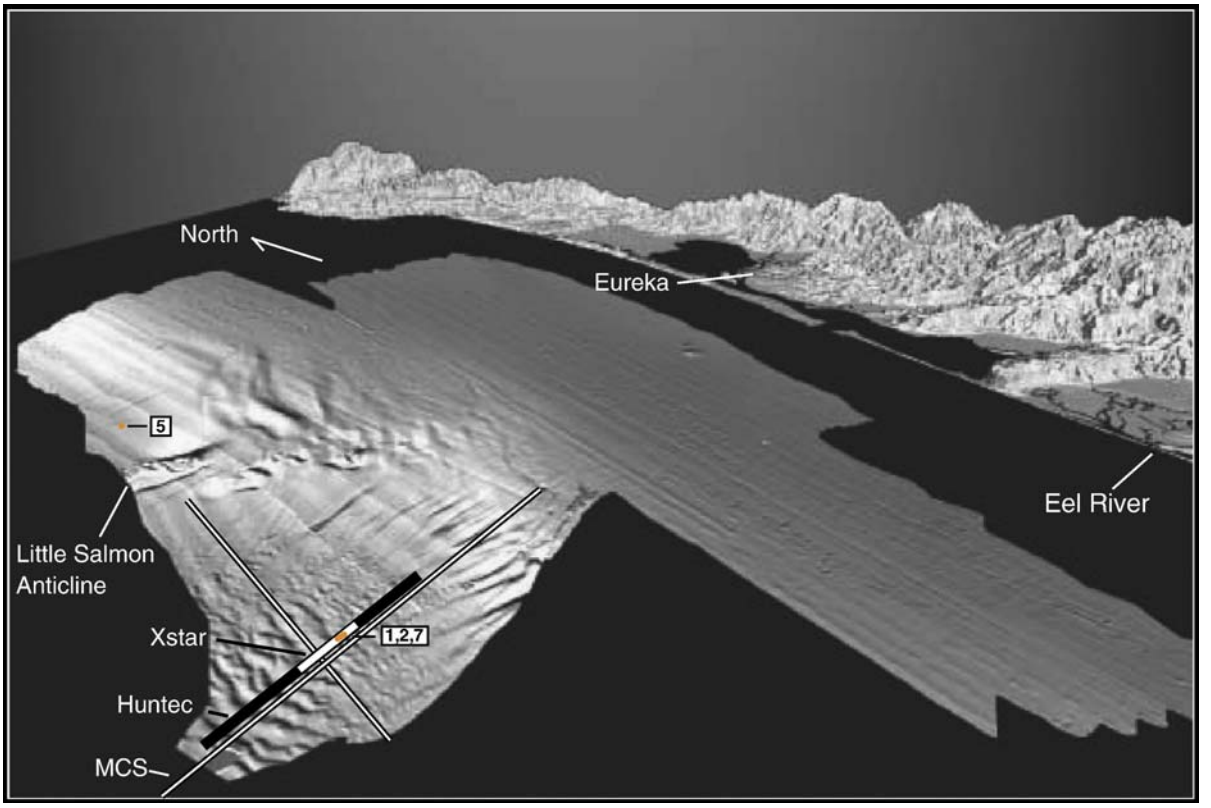

Fig. 2. Location of XStar CHIRP (Fig. 4), Huntec (Fig. 5), and multi-channel seismic (MCS; Fig. 19) lines on the Humboldt Slide amphitheater. The core locations are marked with orange dots. Cores 1, 2 and 7 are coincident with the Chirp, Huntec, and MCS E–W lines. Core 5, which was acquired outside of the Humboldt Slide, was used as a control core for the study. Image courtesy United States Geological Survey.

3. Methods

3.1. Sedimentary AMS fabrics

Early workers such as Ising (1942), Rees (1961), and Marino and Ellwood (1978) suggested the use of AMS to test the reliability of natural remanent magnetism (NRM) measurements from sediments. From these measurements, they concluded that "normal" (oblate) AMS fabrics should generally yield robust results for paleomagnetic field studies. They found poor or incorrect results from samples that showed distorted magnetic fabrics and suggested a wide range of possible causes, including slumping.

Kanamatsu et al. (2001) summarized the potential ways that AMS fabric could be altered by internal (mineralogical) changes and physical reorientation of magnetic grains. Internal changes may be from magnetostriction, growth or dissolution, and brittle or plastic deformation of individual grains. Physical reorientation can be non-coaxial (simple) shear or compaction, which does not alter the fabric within each grain; however, the strain will still alter the overall magnetic fabric.

A range of laboratory experiments have been conducted to examine the depositional controls on magnetic fabrics. For example, Rees and Woodall (1975) investigated a variety of materials using both running-water deposition and deposition from slurries slumping. The experimental results suggest a systematic variation in the AMS fabric with changes in the critical shear stress in the bottom boundary layer (i.e., increasing water current velocity). Additional experiments with plaster mixtures

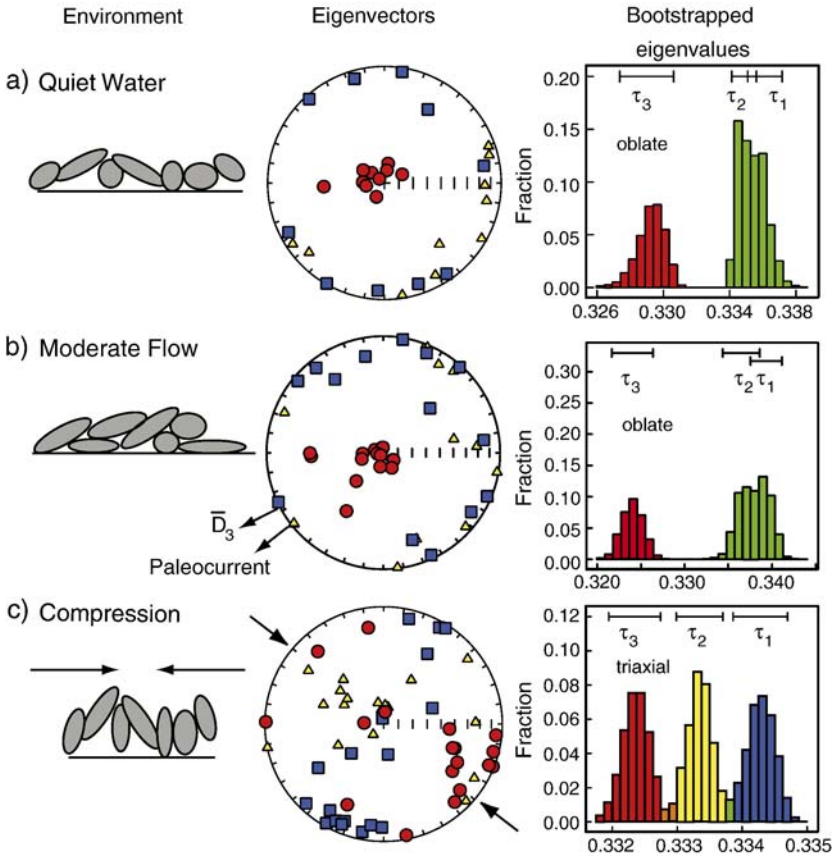

Fig. 3. Schematic diagram illustrating development of sedimentary magnetic anisotropy fabric. Eigenvector directions are plotted in the equal area projections whereby circles are the directions V_3 associated with the minimum eigenvalue τ_3, triangles are V_2 associated with τ_2 and squares are the directions V_1 associated with the maximum eigenvalue τ_1. The histograms to the right are bootstrapped eigenvalues for the specimens showing the 95% confidence intervals for τ_1, τ_2, τ_3. a) Quiet water: the V_3 directions are typically vertical and τ_1 and τ_2 are not significantly different (i.e., the fabric is oblate). b) Moderate flow: the V_3 directions are deflected from the vertical by the current, but the fabric is still typically oblate. The bootstrap mean declination for V_3 ($\bar{D}_3$) is the inferred direction of flow, which closely approximates the paleocurrent direction measured from ripples (Schwehr and Tauxe, 2003). c) Uniaxial horizontal deformation: the eigenvalues will be significantly different (i.e., the fabric is triaxial). In extreme cases, the V_3 directions will ultimately become horizontal. Arrows show the direction of compression that is orthogonal to the V_1 orientation. Note that scales vary for the histograms.

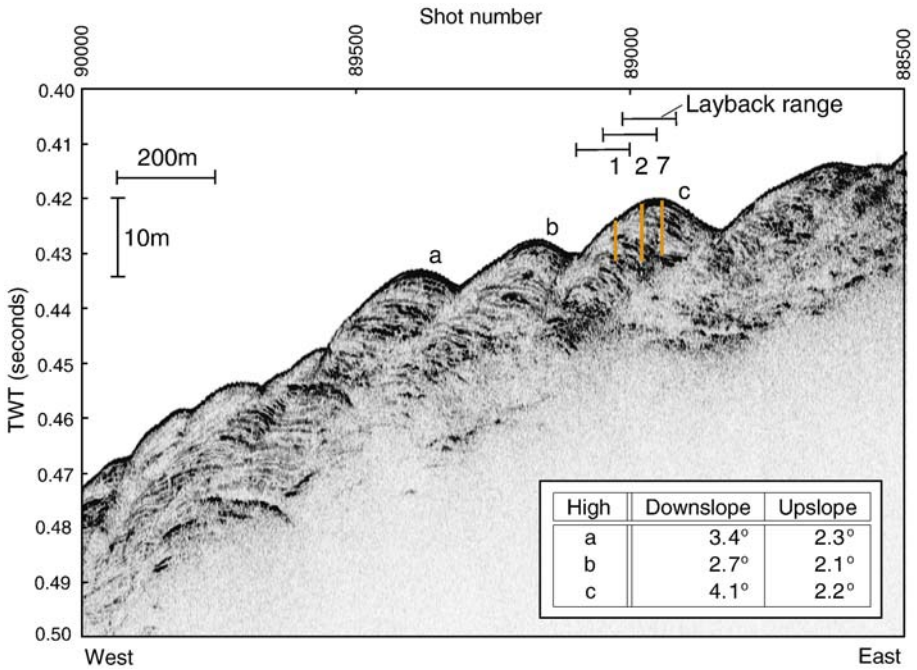

Fig. 4. EdgeTech XStar CHIRP seismic line collected in 1999 (See Fig. 2). This 1681 m long line trends NW–SE and images three prominent highs with internal reflectors (labeled a–c). Two way travel time is in seconds. Layback is calculated using wire angle and fish depth. The error bars are shown for wire angles ranging from 30 to 45° with the cores located at a wire angle of 35°, which is why the error bars are not symmetric with respect to the cores. The inset table shows the seafloor slopes of the three prominent highs that are labeled a–c on the CHIRP seismic line.

found that the eigenvector associated with the maximum eigenvalue can align either parallel or perpendicular to flow direction depending on flow conditions (Rees, 1983).

Several authors have recognized the effects of sediment deformation on NRM (see Tarling and Hrouda, 1993 and Tauxe, 1998 for summaries). For example, Rosenbaum et al. (2000) examined a core (OL-92) from Owens Lake, CA that contains sediments ranging from 800 ka to the present. The original interpretation of the OL-92 magnetic record was that there were a number of geomagnetic excursions in the Brunhes Chron (Glen and Coe, 1997). Rosenbaum et al. (2000) found that sediment deformation was associated with a number of these "excursions" and that the eigenvector associated with the minimum magnetic susceptibility (here called V_3) could be used as an indicator for deformation. If the direction of V_3 is significantly deflected from vertical, that portion of the core might have been deformed, and therefore should not be used for field direction or field intensity. Rosenbaum et al. (2000) arrived at the conclusion that the deformation observed in the OL-92 core was a result of fluidization. A seismic survey conducted after coring shows that the OL-92 core is located in the Owens Valley Fault Zone (Brooks and Johnson, 1997) and the deformation could have resulted from a combination of drilling and faulting.

Given that AMS is extremely sensitive to strain (Housen et al., 1996; Kanamatsu et al., 2001), magnetic fabric has recently been used to detect subtle deformation of sediments and to distinguish geomagnetic features from deformational artifacts (e.g., Rosenbaum et al., 2000; Cronin et al., 2001). Cronin et al. (2001) suggested that AMS could be used to detect slumps not otherwise obvious from the geologic field evidence (so-called "crypto-slumps", Schwehr and Tauxe, 2003). These studies show that AMS can distinguish between post-depositional deformation and primary depositional features. Although AMS has long been used to detect deformation in a variety of geological applications, our aim is to determine the geological origin of a continental margin deposit. AMS may provide a powerful method that can be used in a number of geological settings to detect post-depositional deformation where existing data are equivocal.

There is always the possibility that there might be complications in the AMS results caused by diagenetic effects on the magnetic mineralogy. Such changes can be detected using rock magnetic methods such as anhysteretic remanent magnetization (ARM), isothermal remanent magnetization (IRM), low field bulk susceptibility (χ_{lf} or sometimes written just χ) and high field susceptibility χ_{hf} (e.g. Banerjee et al., 1981; King

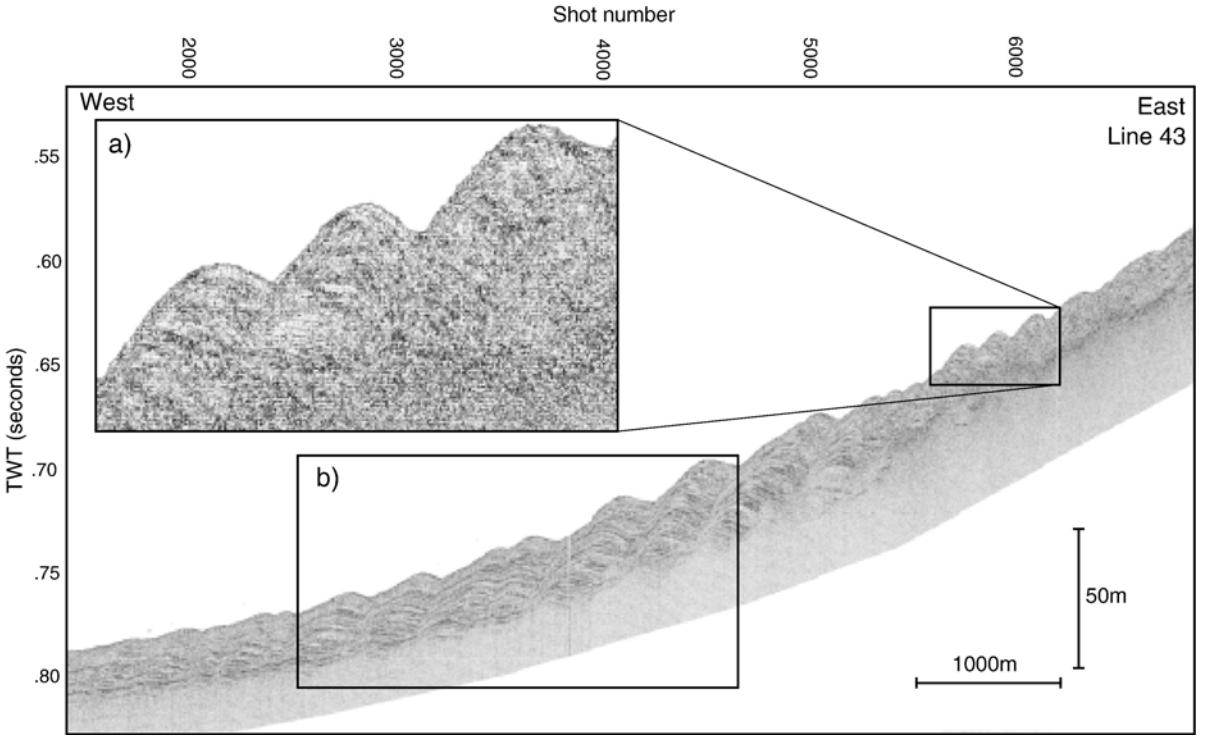

Fig. 5. Huntec seismic line collected in August 1995 on cruise W-2-95-NC. The line trends NW–SE across the structure and is from Gardner et al. (1999). Line 43 is 6086 m long, with the inset (region a) covering 910 m. Two way travel time is in seconds. Region a images the three structural highs that are shown in Fig. 4. Region b images a drape that is much thinner upslope in region a, the location of the cores (modified from Fig. 4 of Gardner et al., 1999).

et al., 1982; Karlin, 1990a; Leslie et al., 1990a; Tauxe et al., 2002; Egli, 2004).

3.2. Development of magnetic fabric in sediments

Here we summarize decades of research on AMS fabric in sediments in a variety of current regimes (see Fig. 3; Tarling and Hrouda, 1993). In quiet water conditions (Fig. 3a), there is a tendency for elongate particles to lie sub-parallel to the bedding plane. As the magnetic susceptibility is usually at a maximum parallel to the long axis of particles, the direction of maximum magnetic susceptibility (V_1) will tend to lie close to the plane of the bedding. However, there is no preferred direction within the bedding plane, therefore the direction of intermediate magnetic susceptibility (V_2) and V_1 will be indistinguishable as will the associated eigenvalues (τ_2 and τ_1). Hence, the magnetic fabric will be oblate with a vertical V_3 direction.

In moderate water currents (Fig. 3b), especially on inclined bedding planes, particles may be slightly deflected, resulting in off-vertical V_3 directions. Here too, we expect the fabric to be characterized by an oblate AMS ellipsoid, but the V_3 direction will be deflected in the direction of the paleocurrent.

What happens to the magnetic fabric during post-depositional deformation is more complex. Initial theoretical work on the relationship between magnetic fabrics and actual grain fabrics with respect to strain was conducted by Owens (1974), Hrouda and Hruskova (1990), and Housen et al. (1993). Most studies using AMS fabric to determine strain have been applied on tectonic scales and have examined weakly metamorphosed rocks (e.g. Pares et al., 1999; Kanamatsu et al., 2001). Studies on such low-grade metamorphic rocks are complicated because chemical changes during metamorphism may affect the magnetic minerals to

Table 1
Cores 1, 2, and 7 were collected in the center of the Humboldt Slide

Core	Latitude	Longitude	Water depth (m)
1	124° 30″ 09.96′ W	40° 50″ 20.16′ N	460
2	124° 30″ 07.62′ W	40° 50″ 19.86′ N	460
5	124° 27″ 12.08′ W	40° 59″ 00.30′ N	419
7	124° 30″ 05.84′ W	40° 50″ 19.87′ N	461

Core 5 was collected to the north of the slide.

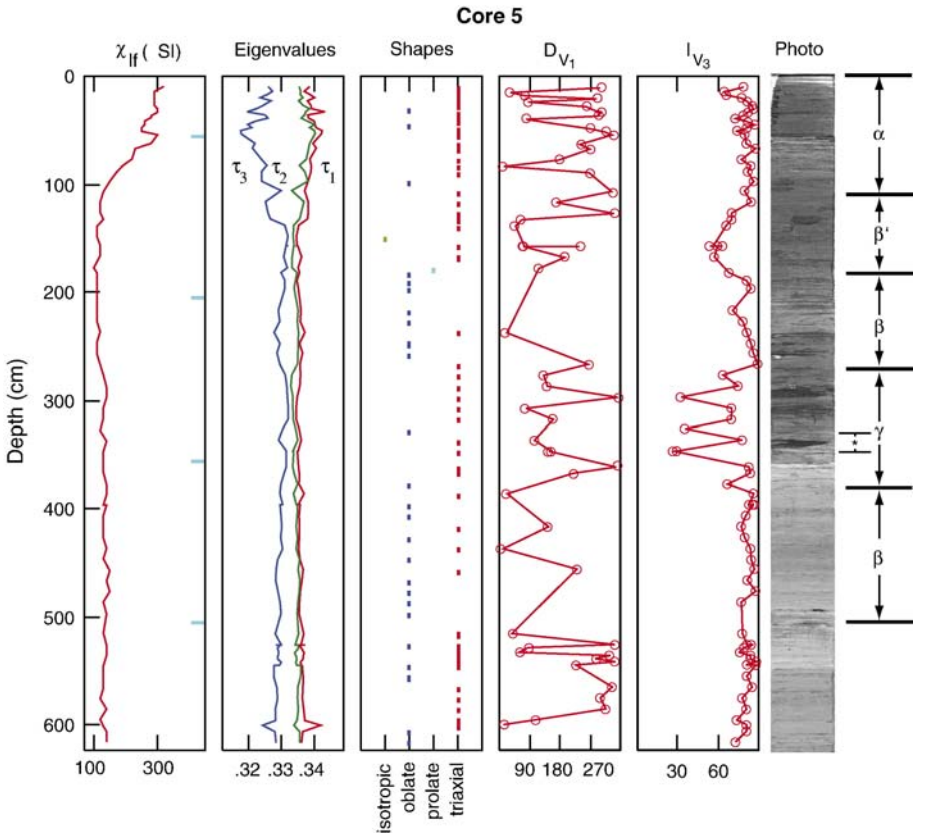

Fig. 6. Piston core 5 is located north of the Humboldt Slide as a control core. Down core measurements of bulk susceptibility (χ_{lf}), eigenvalues, fabric type (as illustrated in Fig. 3), D_{V_1} (declination of the major eigenvector), and I_{V_3} (inclination of the minor eigenvector) are shown. The majority of samples show triaxial fabric suggesting deposition under strong flow conditions. There is no systematic pattern in the D_{V_1}, but there is a zone from 270 to 380 cm (γ zone) where I_{V_3} differs significantly from vertical, which could possibly be a slump or extreme flow conditions. See Fig. 16 for an enlarged view of the region delineated by the (*) to the right of the core photo in the γ region, which appears to be a recumbent fold. The core photo shows that the γ region of shallow I_{V_3} is located just above the transition from overlying darker sediment to the underlying lighter sediments. Vascular plants are concentrated in the upper darker regions. (For interpretation of the references to color in this figure legend, the reader is referred to the web version of this article.)

some degree. It is difficult to separate physical from chemical effects on magnetic fabrics. Nonetheless, research shows that strain alters magnetic fabric and can have effects such as deflecting the minimum susceptibility vector from vertical, and aligning the maximum eigenvector perpendicular to the axis of compression (see Fig. 3c). By working with sediments that have not experienced diagenesis from deep burial and heating, chemical changes should be minimal.

3.3. AMS and slumping

Cronin et al. (2001) investigated a section of limestone in Italy to define the paleomagnetic field in the Cretaceous Normal Supercron. The paleomagnetic data displayed several intervals in which the direction deviated significantly from the expected normal direction. Such data are often interpreted as excursions of the geomagnetic field. In order to rule out slumping as a possible cause, they used AMS fabrics to characterize the "ordinary" and "deviant" intervals. The deviant intervals were triaxial, while the ordinary intervals were oblate. These results strongly suggest that the deviant directions were the result of crypto-slumping, which is soft sedimentary slumping sub-parallel to bedding that leaves little to no visible record in the outcrop.

As suggested by Rosenbaum et al. (2000) and Cronin et al. (2001), it appears that even minor amounts of soft sediment deformation can have a profound effect on the paleomagnetic record. However, such deformation can be extremely difficult to detect based on visual observations alone, hence the term crypto-slump (Schwehr and Tauxe, 2003).

Schwehr and Tauxe (2003) pursued the idea that soft sediment deformation can be detected through the use of AMS by investigating both crypto-slumped sediments

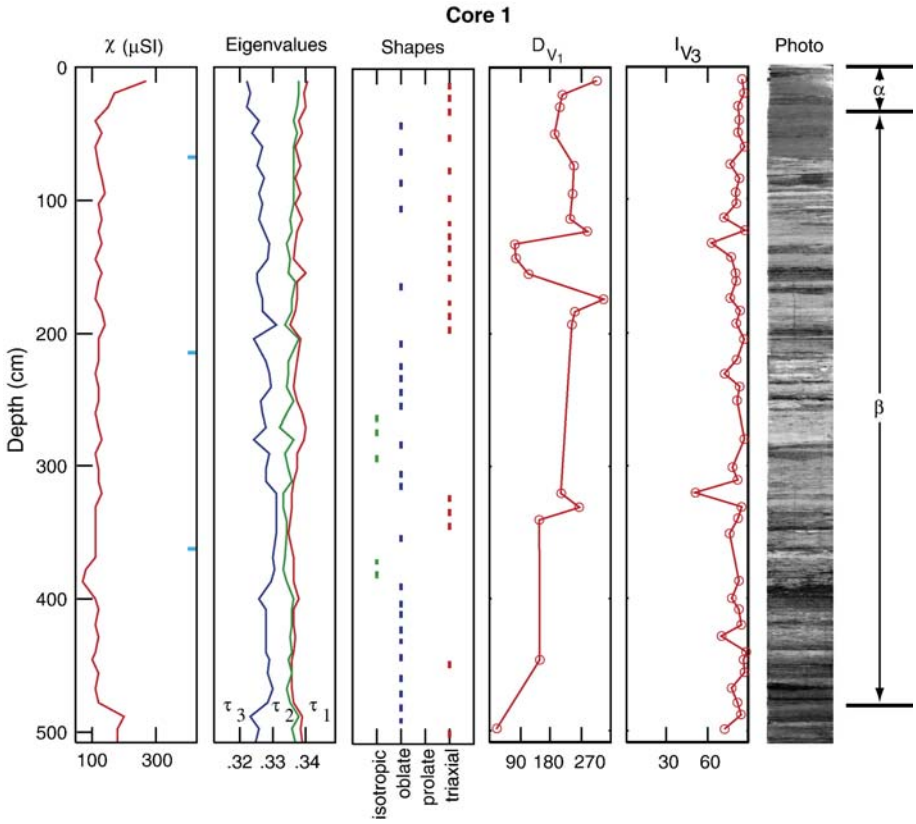

Fig. 7. Piston core 1 is located on the downslope limb of the wave structure. Note that the upper 200 cm of the core appears triaxial, whereas beneath this, the sample fabrics are predominantly oblate. The eigenvalues suggest a systemic decrease in the overall anisotropy down core. The density of V_1 and V_3 measurements compared to the number of samples in the shapes column appears low because many samples failed to pass the 95% F-test (Hext, 1963). The ticks on the right side of the χ_{lf} graph mark the boundaries where the core was cut into sections.

from a marine environment, along with the sediments from within and above the slump to confirm observations of Cronin et al. (2001). They found a crypto-slump in a shale that can be traced laterally to a slumping event observed in the outcrop. Without the excellent exposure and lateral continuity along the outcrop, its slumped nature would not be easily detected. Schwehr and Tauxe (2003) then developed a test for post-depositional deformation based on the AMS characteristics of slumped versus undeformed sediments.

In essence, the test assesses whether the V_3 directions are vertical and distinct from V_1 and V_2, and whether the fabric is oblate (as expected for undisturbed sediment), or triaxial or prolate (as expected for disturbed fabrics). They used a statistical bootstrap approach to perform this test (see Constable and Tauxe, 1990; Tauxe, 1998 for more details).

The example from Schwehr and Tauxe (2003) shows that AMS is able to distinguish between sedimentary structures and deformation in situations where field observations are ambiguous. However, the AMS bootstrapping technique developed by Cronin et al. (2001) and Schwehr and Tauxe (2003) may not be easily applicable to cores such as those collected in the Eel River Basin because of different compaction and deformation states. Bootstrapping conducted by Cronin et al. (2001) and Schwehr and Tauxe (2003) grouped samples into stratigraphic layers; however, such sampling is not currently possible with today's coring technology. For each stratigraphic layer, there may be different magnetic grain distributions and concentrations in addition to the possibility of different flow regimes and directions. We employ bootstrap statistics on sediment zones in this study, but the results should be used with caution.

3.4. AMS applied to the Humboldt Slide

The two alternative hypotheses for the formation of the Humboldt Slide deposit (slope failure and sediment waves) predict very different fabrics that can be measured using AMS. The deformational hypothesis of Gardner et al. (1999) predicts a triaxial fabric with the

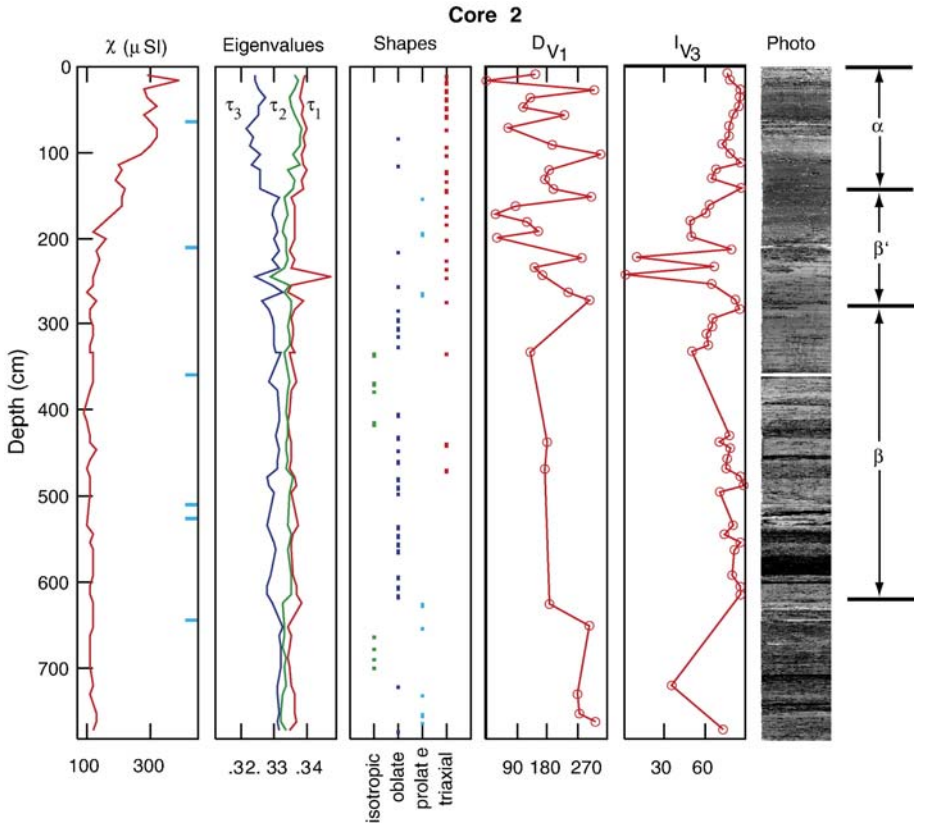

Fig. 8. At 100 cm core depth in piston core 2, there is shift in both χ_{lf} and the eigenvalues that culminates at approximately 190 cm. This shift suggests two different sediment sources. Underlying this transition is a region that appears to be deformed (or have been deposited under high flow conditions) from 160 to 280 cm. Pervasive deformation throughout the core is not observed.

maximum axes of susceptibility (the V_1 eigenvectors) being either poorly grouped, perpendicular to the most compressive stress (see Fig. 3c), or approximately north-south. The density current hypothesis of Lee et al. (2002) predicts oblate fabrics with the minimum axis of susceptibility (projected into the lower hemisphere) deflected in the direction of paleocurrent flow (see Fig. 3b), or approximately westward. The center region of the core should display oblate AMS fabric if the features are depositional, whereas broad deformation will show dominantly triaxial fabric throughout.

3.5. Seismic data

Seismic lines covering the top half of the Humboldt Slide were acquired during August 1999 as part of the ONR STRATAFORM project (cruise TTN-096). The CHIRP seismic system (e.g. Schock et al., 1994; Quinn et al., 1998; Gutowski et al., 2002) is a modified EdgeTech XStar system with an ADSL link from the fish to the topside computers. The data were collected with a 50 ms sweep from 1 to 6 kHz. The XStar SEG-Y records were processed with seismic-py and SIOSEIS (Henkart, 2006), and were plotted with pltsegy. Fig. 4 shows the section of the cruise data relevant to this study.

The Huntec data presented in Fig. 5 were collected during August 1995 on cruise W-2-95-NC. The data were processed with a combination of Sonarweb and seismic-py. A hydrophone (channel 2) is mounted on a tail behind the fish, which experiences a large amount of motion, so we processed only channel 1 (Galway, 2000). Huntec data from cruises W-2-95-NC and W-1-96-NC have been presented in Gardner et al. (1999) and Lee et al. (2002).

3.6. Coring

In November 2001, large-diameter piston cores were acquired using the Oregon State University Coring Facility on board the *R/V Thompson*. The core sites were selected based on CHIRP seismic data (Fig. 4) and on EM-1000 swath bathymetry (Fig. 2). P-code differential GPS was used to locate the core sites and yielded 10 m, or better, accuracy of the core location. Core locations and lengths are summarized in Table 1.

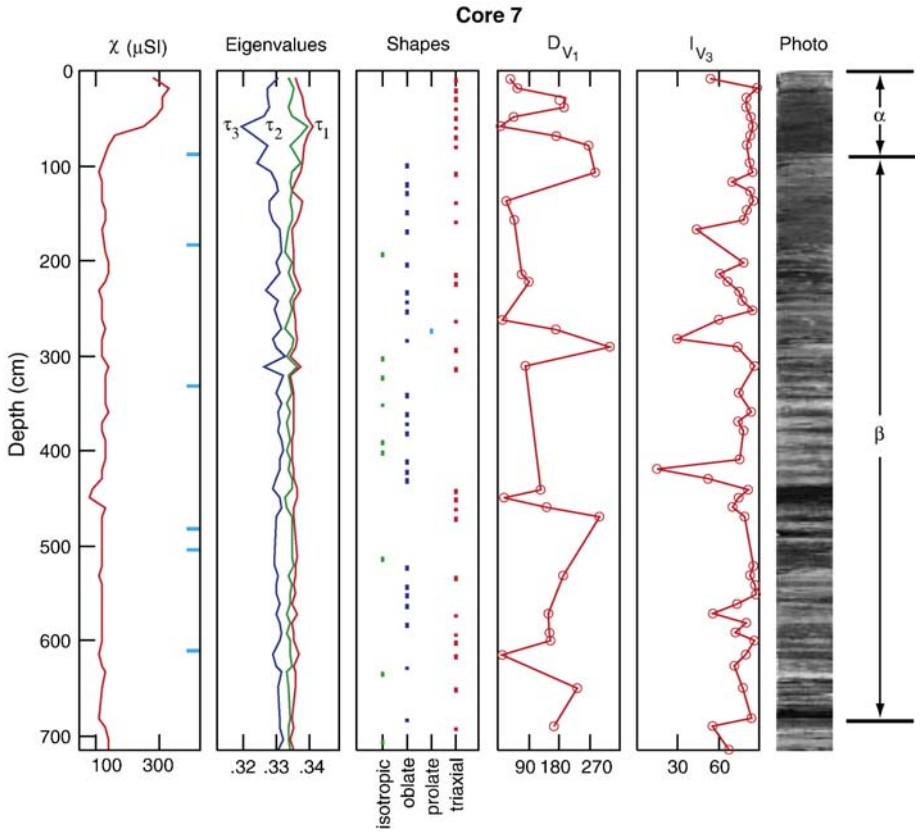

Fig. 9. Piston core 7. This core has the same shift in χ_{lf} observed in the other piston cores. There is no discernible trend in the D_{V_1}. The I_{V_3} shows a section with non-vertical vectors, but this is a small region and many of the samples are isotropic.

The lengths of the piston cores range from 5.9 to 7.8 m. The piston cores have an inner diameter of 10.2 cm which minimizes deformation associated with coring allowing undisturbed samples for AMS analysis to be acquired away from the liner effects.

Core 5 (Figs. 2 and 6), collected north of the Humboldt Slide, serves as a control because it is located in an area with minimal deformation based on the seismic and bathymetric data. Core 5 was collected at a depth similar to that of cores 1, 2, and 7 and is located in a portion of the slope characterized by gullies (referred to as rills) described by Spinelli and Field (2001). We predicted that the AMS results for the control core would show a normal sedimentary fabric, perhaps with a signature of current flow down or across slope (i.e., gravity sheet flows or slope-parallel contourites).

Cores 1, 2, and 7 were acquired in the primary study site within the Humboldt Slide (Figs. 4 and 7–9). These cores sampled across the crest of one sedimentary structure located in the center of the Humboldt Slide at a water depth of 460 m. This feature has a wavelength of about 150 m and an amplitude of approximately 6 m. Given fish layback uncertainty (as marked in Fig. 4), it is not possible to determine exactly where on these structures each core was acquired; however, it is clear that the three cores have sampled both the upslope and downslope components of the slide on feature c. Note that the estimated core penetration is shown on Fig. 4.

3.7. Paleomagnetics

From the cores, we collected 8 cm^3 paleomagnetic sample cubes with a typical sampling interval of 10 cm. The down core AMS measurements provide the key data for interpreting the Humboldt Slide as either a retrogressive failure or a downslope current-controlled deposit (i.e., sediment waves) infilling a slide scar. Magnetic measurements were performed at the Scripps Paleomagnetic Laboratory. NRM measurements were conducted on 3-axis CTF and 2-G cryogenic magnetometers (designated Bubba and Flo respectively), located in a magnetically shielded room. Alternating field (AF) demagnetizations were accomplished using an SI-4. After best fit directions for each sample were found, the Fisher statistics (Fisher, 1953) were applied to each core section to get a best fit declination ($\bar{D}$, Table 2).

Table 2
Fisher statistics (Fisher, 1953) of alternative frequency (AF) demagnetization of the natural remanent magnetization (NRM) listed by core sections

Core	Section	$\bar{D}$	$\bar{I}$	N	R	κ	α_{95}	Depth (cm)
1	1	217.2	67.5	6	5.3555	7	25.7	69
1	2	335.6	56.3	12	11.4192	18	10.2	216
1	3	319.3	49.5	12	10.8026	9	15.1	363
1	4	338.6	55.4	12	11.4111	18	10.3	508
2	1	85.0	58.7	4	3.9492	59	12.1	62
2	2	322.7	70.8	13	12.5929	29	7.8	209
2	3	279.3	62.0	11	10.4484	18	11.0	358
2	4	251.1	64.3	9	8.8349	48	7.5	507
2	5			0				525
2	6	293.5	68.0	5	4.8824	34	13.3	642
2	7	124.8	49.2	7	6.8468	39	9.8	783
5	1	132.1	36.8	13	12.8963	115	3.9	57
5	2	208.2	49.9	19	16.8045	8	12.5	207
5	3	225.9	49.9	3	2.9145	23	26.1	356
5	4	220.9	68.8	3	2.9699	66	15.2	505
5	5	254.9	66.8	7	4.7290	2	46.4	624
7	1	17.6	58.1	5	4.8088	20	17.1	87
7	2	39.7	63.5	7	6.7688	25	12.1	182
7	3	38.2	71.3	13	12.0803	13	11.9	330
7	4	67.8	58.5	13	11.5771	8	15.2	481
7	5			0				502
7	6	214.1	63.7	10	9.1058	10	16.0	610
7	7	224.8	57.4	8	7.7080	23	11.5	755

The declination is in the core section local frame before reorientation to geographic north. Based on a Geocentric Axial Dipole (GAD) model, the expected inclination for these cores is 60.0°. *Note*: $\bar{D}$ is the mean declination; $\bar{I}$ is the mean inclination; N is the number of specimens; R is the length of resultant vector; κ is the Fisher (1953) precision parameter; and α_{95} is the estimate of the circle of 95% confidence. The α_{95} values are too large to detect rotations smaller than 4.1° (2.1–4.1° observed in CHIRP seismic data – Fig. 4). Depth is the distance below the core top to the bottom of the core section.

$\bar{D}$ was then applied to each core section such that the AMS eigenvectors are geographically oriented. AMS was measured on a Kappabridge KLY-2 using the same approach as is outlined in Schwehr and Tauxe (2003). ARM acquisition was accomplished with a SI-4 using a 100 mT alternating field and a 40 μT bias field. IRM's were imparted with an ASC impulse magnetizer with a field of 1 Tesla.

A best fit tensor is derived from the 15 measurements made on the KLY-2 Kappabridge as a part of the AMS acquisition. A bulk susceptibility (χ_{lf}) is calculated, and the eigenvalues presented are normalized to sum to 1. To determine the fabric shape, we use the F statistics of Hext (1963) (see also Tauxe, 1998). The F test checks for overall significance of anisotropy. If F_{ij} is below the 95% threshold for significance, the eigenvalues τ_i and τ_j are considered indistinguishable. Isotropic samples fail the F_{12} and F_{23} tests, therefore, all three eigenvalues are indistinguishable (Fig. 6: Shapes 1st sub-column — colored green). If the sample is anisotropic, then the F_{12} test checks for significance of the maximum and intermediate eigenvalues and F_{23} for the intermediate and minimum eigenvalues. Oblate samples (2nd sub-column — colored blue) have τ_2 and τ_3 that are significantly different, whereas prolate samples (3rd sub-column — colored cyan) have τ_1 and τ_3 being significantly different. If the sample passes both F_{12} and F_{23}, then all three eigenvalues are distinct and the sample is termed triaxial (4th sub-column — colored red).

The V_1 declination (D_{V_1}) shows the direction of the eigenvector associated with the maximum eigenvalue. This direction is only meaningful if the τ_1 eigenvalue is statistically distinguishable from τ_2. Therefore, the V_1 directions marked as prolate (cyan) and triaxial (red) in the Shapes column are significant. V_1 tends to be associated with the long axis of the magnetic grains. The V_3 inclination is meaningful when the fabric shape is either oblate or triaxial (τ_3 distinct from τ_2). The inclination of V_3 (I_{V_3}) is often used as a proxy for detection of bed rotation (e.g. Rosenbaum et al., 2000; Kanamatsu et al., 2001; Housen and Kanamatsu, 2003).

After magnetic measurements were made, the samples were wet sieved to remove the clay to medium silt fraction using a 47 μm screen. Finally, a range of grain size separates were sieved to determine silt, sand, and organic debris fractions; the organic debris included branches, twigs, seeds, etc.

4. Results

Cores 1, 2, and 7 were collocated with CHIRP seismic data to constrain the geometry and stratigraphy of the three prominent highs being studied (marked a–c in Fig. 4). These three cores were collected across high c. The seismic reflection data were used to determine where to sample the features because in certain areas the deformed features are mantled by a pelagic drape. The thickness of the drape varies systematically from the top of the slide complex to the base (Fig. 5). At the top of the slide structure, there is little to no detectable pelagic drape overlying the deformed features at the locations of cores 1, 2, and 7 as observed in the CHIRP and Huntec seismic lines (Figs. 4 and 5a). Examination of our core locations (Fig. 4) and co-registered seismic data reveal that all three cores penetrated through any pelagic drape into the underlying sedimentary features.

The CHIRP system imaged faint seaward dipping reflectors with high-amplitude landward dipping reflectors. There is a marked asymmetry with the landward dipping sequences being much thicker than the seaward dipping units. In fact, across some features only the landward

Table 3
Bootstrap statistics for each zone type

Core	Zone	V	$\bar{D}$	$\bar{I}$	η	D_η	I_η	ζ	D_ζ	I_ζ
1p	α	V_1	191.3	1.7	4.4	78.0	85.6	90.0	281.5	4.0
2p	α	V_1	169.1	5.1	9.0	309.9	83.5	90.0	78.7	4.1
5p	α	V_1	296.0	2.7	5.9	179.3	84.0	90.0	26.3	5.4
7p	α	V_1	213.4	1.9	10.3	355.8	87.7	77.5	123.3	1.4
1p	α	V_3	81.9	84.8	3.3	172.2	0.0	4.8	262.2	5.2
2p	α	V_3	306.1	83.1	6.3	86.6	5.4	7.5	177.0	4.4
5p	α	V_3	180.0	83.9	5.0	304.9	3.5	6.0	35.2	5.0
7p	α	V_3	18.5	88.1	9.2	198.1	1.9	10.8	288.1	0.0
2p	β′	V_1	154.8	24.4	40.0	316.6	64.5	90.0	61.6	7.0
5p	β′	V_1	52.3	3.6	23.3	302.6	79.3	90.0	142.9	10.0
2p	β′	V_3	325.1	65.3	40.7	155.3	24.4	90.0	63.5	3.9
5p	β′	V_3	302.5	79.4	16.5	89.4	8.9	21.0	180.3	5.7
1p	β	V_1	271.0	2.5	5.6	70.1	87.3	90.0	181.0	1.0
2p	β	V_1	154.3	11.4	9.3	353.5	78.0	90.0	245.1	3.8
5p	β	V_1	25.2	1.4	5.4	270.4	86.7	90.0	115.3	3.0
7p	β	V_1	161.9	0.0	7.6	252.0	83.9	74.6	71.9	6.1
1p	β	V_3	71.3	87.4	4.7	222.5	2.3	5.4	312.6	1.3
2p	β	V_3	347.7	78.3	8.5	171.8	11.7	9.0	81.6	0.8
5p	β	V_3	266.0	87.2	4.2	72.5	2.8	4.8	162.5	0.7
7p	β	V_3	252.0	84.6	6.8	343.2	0.1	8.3	73.3	5.4
5p	β	V_1	329.8	0.5	40.8	236.7	80.7	90.0	59.9	9.3
5p	β	V_3	233.2	85.5	36.3	138.3	0.4	42.5	48.3	4.5

η and ζ are the angle of major and minor axis for the ellipse of 95% confidence. D_η and I_η are the major axis direction, whereas D_ζ and I_ζ are the minor axis direction.

dipping sequences are observed with individual horizons cropping out at the sea floor on the seaward slope (Fig. 4a).

The first test to determine if post-depositional deformation occurred is to examine the NRM directions for evidence of rotation. The seaward and landward limbs of these features (Fig. 4a–c) exhibit a range of dips from 2.1° to 4.1° (Fig. 4: inset table). Cores 1, 2 and 7 penetrate structure c which has a seafloor landward slope of 2.2° and a seaward slope of 4.1°. If there is E–W compression or rotation with a northerly fold axis, there should be a shallowing of approximately 0.5° in the NRM inclination compared to the expected geocentric axial dipole (GAD) inclination of 60.0°. Given that the α_{95} confidence values range from 8 to 26° (Table 2: cores 1, 2, and 7), such small rotations are below the resolution of this approach, and therefore, we must rely on the AMS technique for detecting post-depositional deformation.

The AMS results are shown in Figs. 6–9. Core 5 (Fig. 6) was collected as a control for this study and as such, it is located outside of the Humboldt Slide. Cores 1, 2, and 7 were acquired within the slide feature to assess whether the sediment carapace has experienced rotation and deformation. Based on the observation of the AMS fabric observed in the cores, four distinct zones termed α, β, β′, and γ were identified. Core 5 is used as the "type section" because it exhibits all four zones. Here we will describe the characteristics that define the four zones.

4.1. α — *alpha*

The first zone, α, is characterized by high susceptibility and high anisotropy observed in the AMS data. Individual samples exhibit a predominantly triaxial AMS fabric type with near-vertical orientation of the minor eigenvector (see Figs. 6–9: I_{V_3}). The Hext (Hext, 1963) average inclination of V_3 for a group of samples is recorded in Table 3 as $\bar{I}$. The V_1 eigenvectors, as observed in the equal area projection (Fig. 10), have no preferred orientation (Figs. 6–9: D_{V_1}). The confidence ellipses and best fits derived by bootstrap statistics for the different zones are reported in Table 3. The α zone is also characterized by large ARM, IRM and χ_{lf} (we plot only χ_{lf} in Figs. 6–9). An increase in the coarse silt fraction correlates with the boundary between α and β′ in core 2 (Fig. 11: grain size). When plotting IRM versus χ_{lf}, the different zones can be delineated as shown in Fig. 12. α exhibits high and transitional χ_{lf}, ARM, and IRM, whereas low χ_{lf}, ARM, and IRM are characteristic of the other zones (Fig. 12).

4.2. β′ — *beta prime*

The β′ zone is observed in cores 2 and 5 and is characterized by rotation of the V_3 eigenvectors away from vertical determined for the individual sample

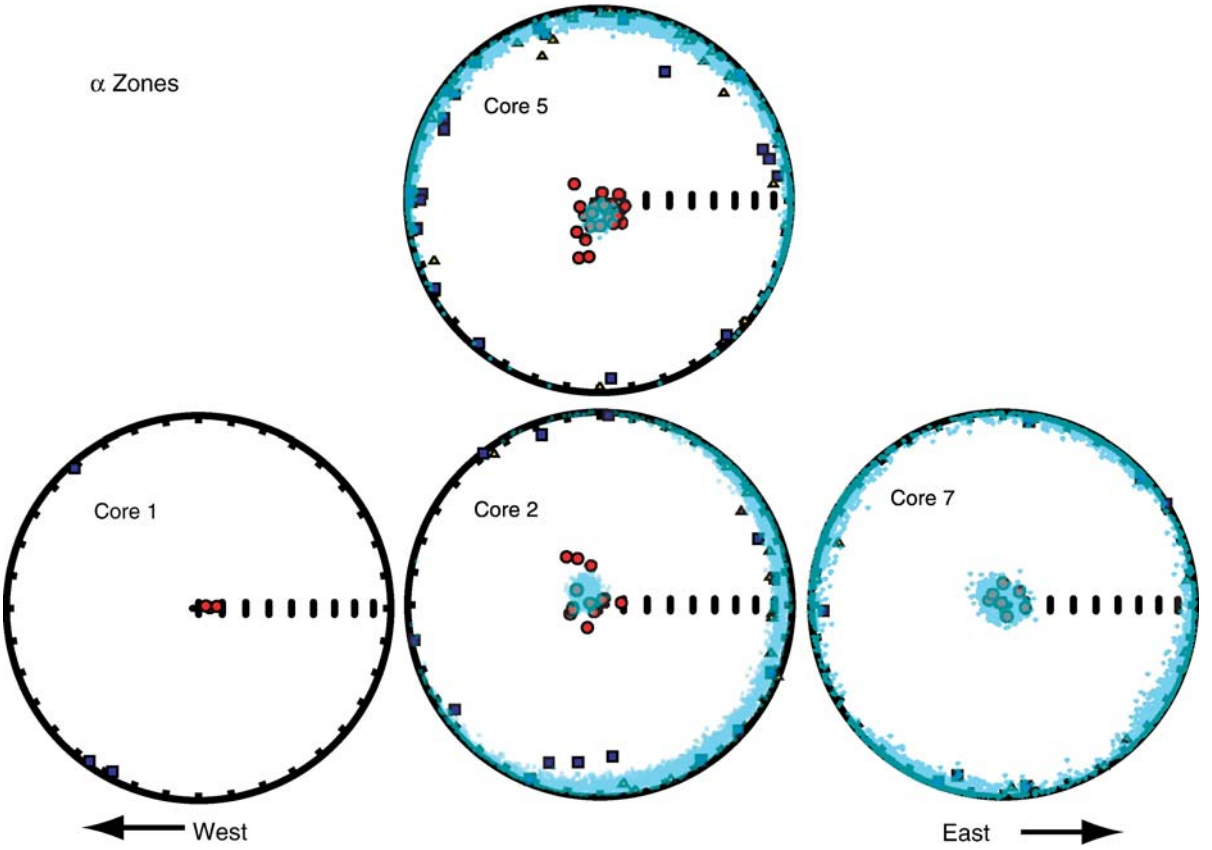

Fig. 10. α zones occur at the top of each of the piston cores. This zone is characterized by high χ_{lf}, anisotropy, ARM, and IRM. The individual shape fabrics are predominately triaxial. Bootstrap eigenvectors have a tight cluster near vertical. Blue squares are V_1; yellow triangles are V_2; and red circles are V_3 . The cyan dots are the bootstrap eigenvectors; V_1–V_3 eigenvectors are not distinguished. (For interpretation of the references to color in this figure legend, the reader is referred to the web version of this article.)

measurements (Figs. 6 and 8: I_{V_3}). The deflection of V_3 away from the vertical is also observed in the equal area projections (Fig. 13). A marked decrease in total anisotropy as evidenced by the eigenvalues is also characteristic of the β' zone. (Figs. 6 and 8). V_1 exhibits slightly more grouping in β' than in the overlying α zone, nevertheless a strong preferred orientation is not observed (Fig. 13). The AMS fabrics for individual samples are predominately triaxial for the β' zone.

4.3. β — beta

Underlying the β' zone in cores 2 and 5, there is a pronounced shift to more oblate fabric for individual samples in the β zone. However, the transition from β' to β is not well defined by either the eigenvalues or χ_{lf}. In cores 2 and 5, the β zone is defined by near-vertical V_3 orientation with tight clustering (Figs. 6 and 8: I_{V_3}). Note that in core 7, even though the eigenvalues by sample show some scatter, the bootstrap vectors show a tight cluster near vertical (Fig. 14).

In cores 1 and 7, β' is not observed and the α zone mantles β. When α directly overlies β, the zones are delineated by a marked shift in χ_{lf} (Figs. 7 and 9). In core 7, a marked decrease in overall anisotropy appears to correlate with the boundary between α and β. In core 1, the decrease in overall anisotropy is more subdued for the transition between α and β (Fig. 7) than in the other cores. In the β zone, V_1 for all cores shows weak grouping; however, there does not appear to be a preferred orientation for β. As mentioned before, β is characterized by low χ_{lf}, ARM, and IRM (Figs. 11 and 12).

In all four cores, only small zones of bioturbation are observed. In general, the layering is clearly visible, and undisturbed as revealed by the core photos. The boundaries between layers are sharp, and mottling and smearing of layer boundaries is not commonly observed. A large number of organic-rich layers are clearly visible in the

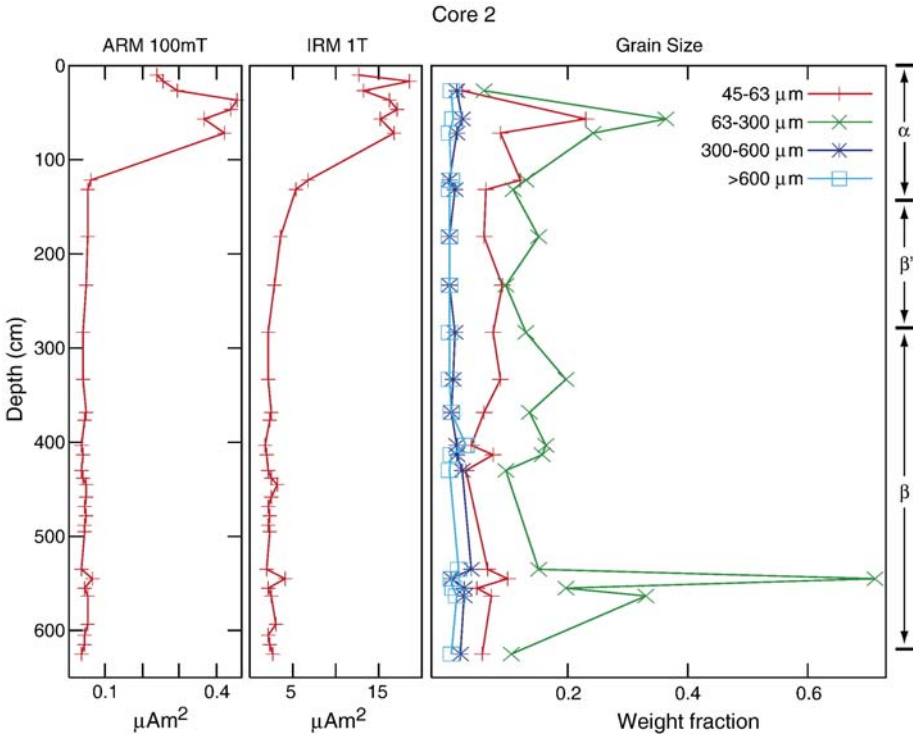

Fig. 11. Anhysteretic remanent magnetization (ARM) and isothermal remanent magnetization (IRM) show an abrupt decrease from α to β'. There is a distinct difference in the ARM and IRM in the first meter of the core. There is a much higher concentration of magnetic grains and a different grain population. The 300 and 600 µm sieves were selected to sort out the vascular planet material, where the >600 µm material is predominantly twigs and branches. The 63–300 µm range captures the sand fraction, while the 45–63 µm range captures the coarse silt fraction.

cores with a maximum thickness of 30 cm (core 2 from 568–589 cm for the vascular plant material deposit; Fig. 6).

The core photos show a reciprocal relationship for the β zone and the occurrence of dark, organic-rich layers depending on whether the cores were acquired within or outside the slide region. Cores 1, 2, and 7 show an increase in occurrence and thickness of dark organic-rich layers in the β zone compared to the α zone. The dark organic-rich layers are comprised mostly of vascular plant matter (Fig. 15). In core 5, the α, β', and upper β zones are characterized by dark organic-rich layers, while the lower beta zone is largely devoid of such layers. In core 5, the thickest dark, organic-rich layers occur in the γ zone (Figs. 6 and 16).

4.4. γ — *gamma*

The γ zone is only observed in core 5, which was acquired to the north of the Humboldt Slide. γ is characterized by a marked deflection of V_3 from vertical in both the individual and group samples (Figs. 6 and 17). In core 5, the β zone above and below the γ zone is characterized by oblate fabric, with γ being predominately triaxial. The γ zone is indistinguishable from β based on χ_{lf}, eigenvalues, ARM and IRM. Within the γ zone, the sediments appear to show signs of post-depositional deformation as a dark, organic-rich horizon may have been folded (Fig. 16: inset).

5. Discussion

In order to fully understand a marine slump, it is helpful to review the features that are typically expected. Comparison with a small slide exhibiting minimal run out shows markedly different features than those observed in the Humboldt Slide. Fig. 18 is a CHIRP seismic image of the Gaviota Slide from the Santa Barbara Basin that exhibits features typical for many slides and provides valuable insights for the expected sedimentary structures and morphology (Schwehr et al., in press). For the Gaviota slide, the failed material has not moved far downslope with minimal translation from the evacuation to accumulation zone. If the failure is retrogressive in origin, then after initiation, the failure propagates upslope from the point of initial failure and terminates at a head-wall scarp. Along the seaward extent of the slide complex, the toe often exhibits signs of compressional deformation (Fig. 18). The V_1 eigenvalues showed a preferred

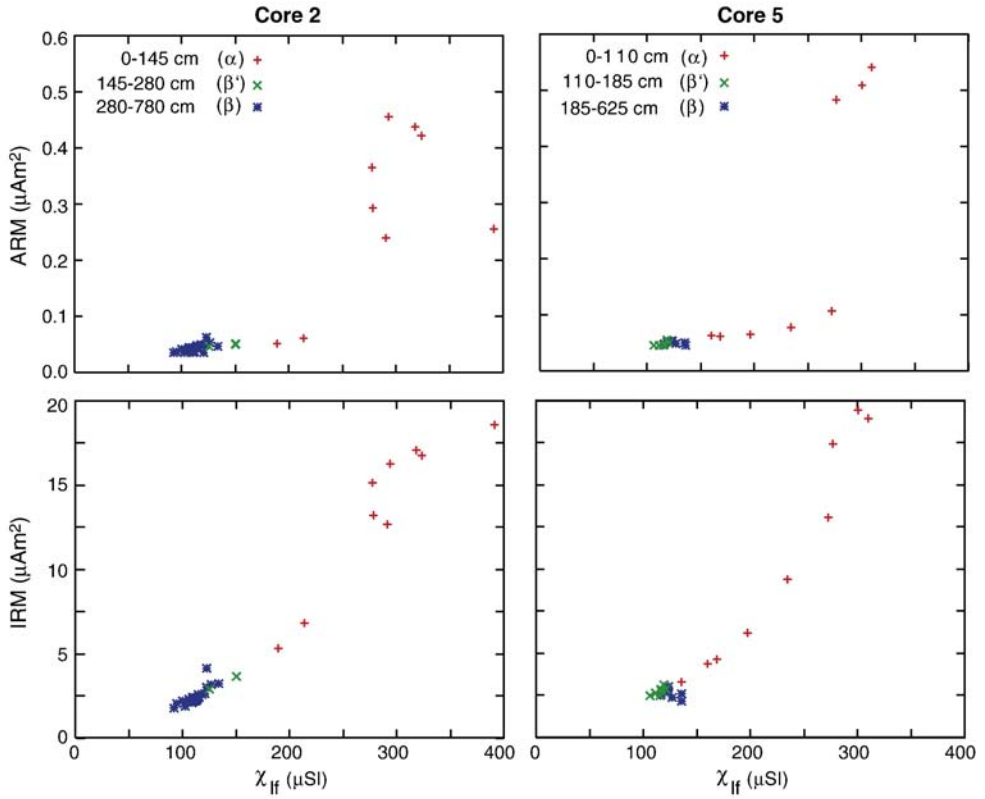

Fig. 12. Core 2 and 5 Banerjee plots. Banerjee et al. (1981) showed that a χ_{lf} versus ARM plot can show grain size for magnetites based on the slope of a line that passes through the origin. In this figure, cores 2 and 5 show three distinct groups. The top of the core exhibits high χ_{lf}, ARM, and IRM with a transition zone in the middle down to the lower χ_{lf}, ARM, and IRM in the deeper section of the core. Comparing to Fig. 11, one can see that shifts in grain size do not necessarily lead to the same change in the magnetic grains.

orientation as a result of downslope compression (Fig. 18: inset). Between the upper headwall scarp and the toe, there is an evacuation zone, where the material has vacated, or a zone of thinned and extended material.

According to Gardner et al. (1999), the Humboldt Slide is thin skinned; however, little or no accommodation zone for this slide is observed. This does not match the model for other slides where either a catastrophic

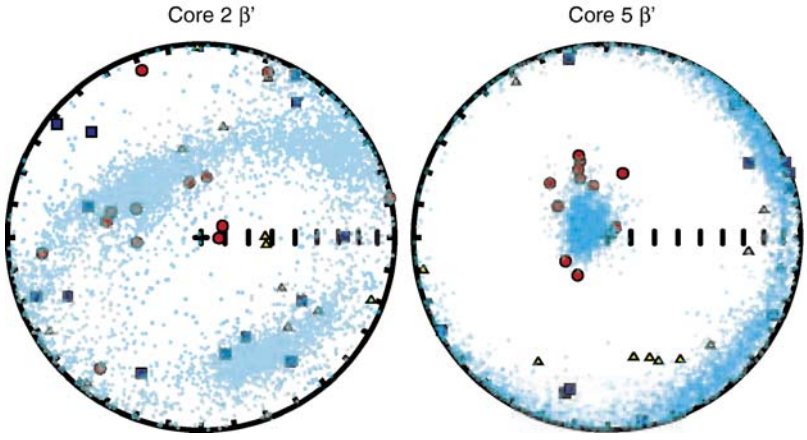

Fig. 13. β' zones occur between α and β and has intermediate values of total anisotropy and bulk susceptibility. The individual shape fabrics are predominately triaxial. Note that there are a number of prolate samples in these two β' zones (see Figs. 6 and 8). Unlike α and β, β' has V_3 vectors that are deflected from vertical.

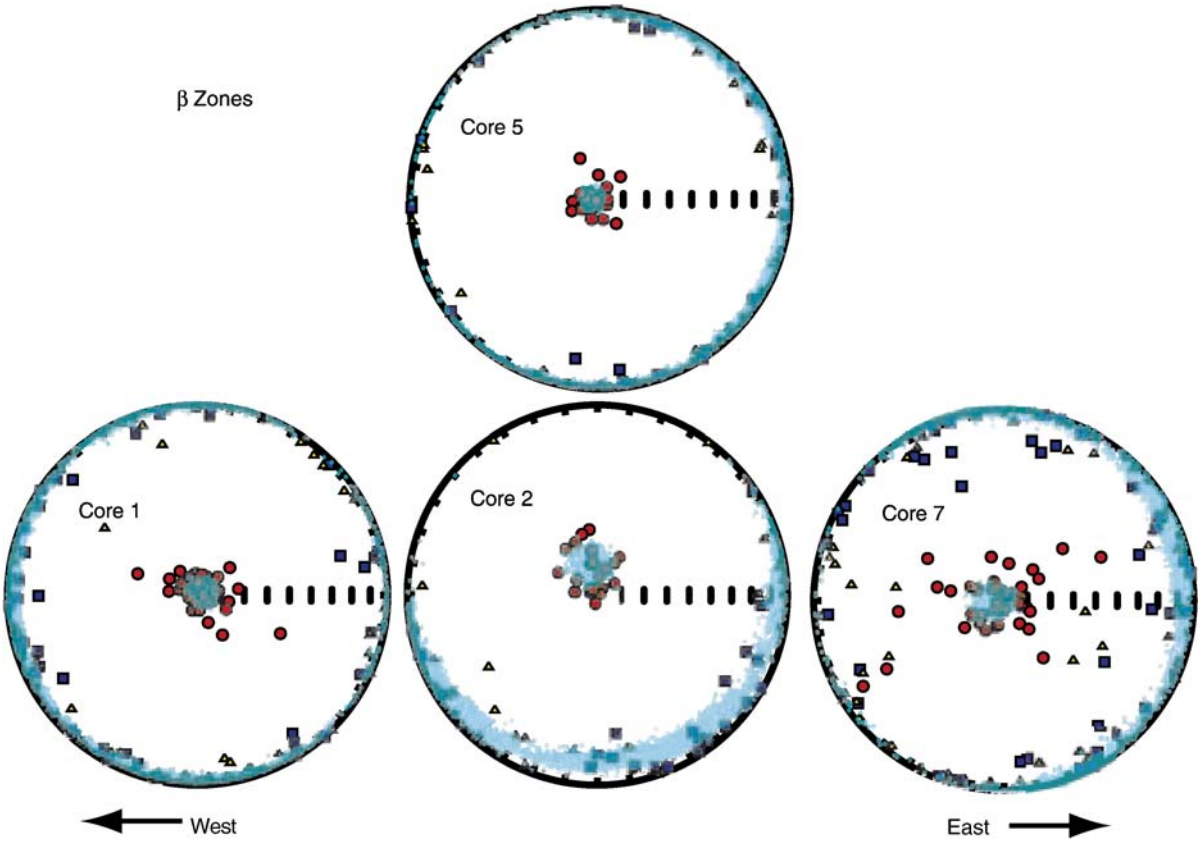

Fig. 14. β zones are characterized by lower anisotropy, ARM and IRM compared the α zones. Individual sample shape fabrics are mostly oblate with some isotropic and triaxial samples. Bootstrap eigenvalues have a tight cluster near vertical. For all except core 7, the V_3 are near vertical. Core 7 has a number of small zones with non-vertical V_3 that may record deposition in a moderate current because there is no preferred orientation for V_1.

failure mobilizes the sediment into a turbidity current, or sediment is removed from an evacuated zone to an accumulation zone downslope (Fig. 18).

The morphology of the Humboldt Slide suggests minimal translation down-slope because there is no downslope thickening or upslope thinning. Furthermore, the MCS data acquired across the region images individual layers that thicken and diverge toward the margin. The divergence of the horizons and the diminished dip up section may reflect long-term tectonic control in the region, suggesting fault-controlled accommodation (e.g., Driscoll and Hogg, 1995). Onlap and thinning are observed across the Little Salmon Anticline.

Lee et al. (2002) presented numerous lines of evidence based on stratal geometry and morphology that the Humboldt Slide features are current-controlled bedforms. Nevertheless, based on the same internal geometry and morphology Gardner et al. (1999) argued that these features are the consequence of post-depositional deformation. As previously mentioned, morphology is not unique and thus, the debate concerning

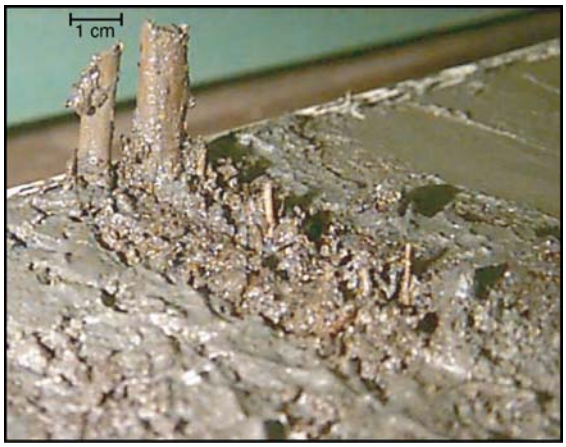

Fig. 15. Oblique photograph of core four inside the Humboldt Slide located at 124° 29.055′ W, 40° 50.106′ N in 419 m of water. The plant matter shown here (at 130 cm from the core top) illustrates frequent flood layers from the Eel River are deposited in the Humboldt Slide region.

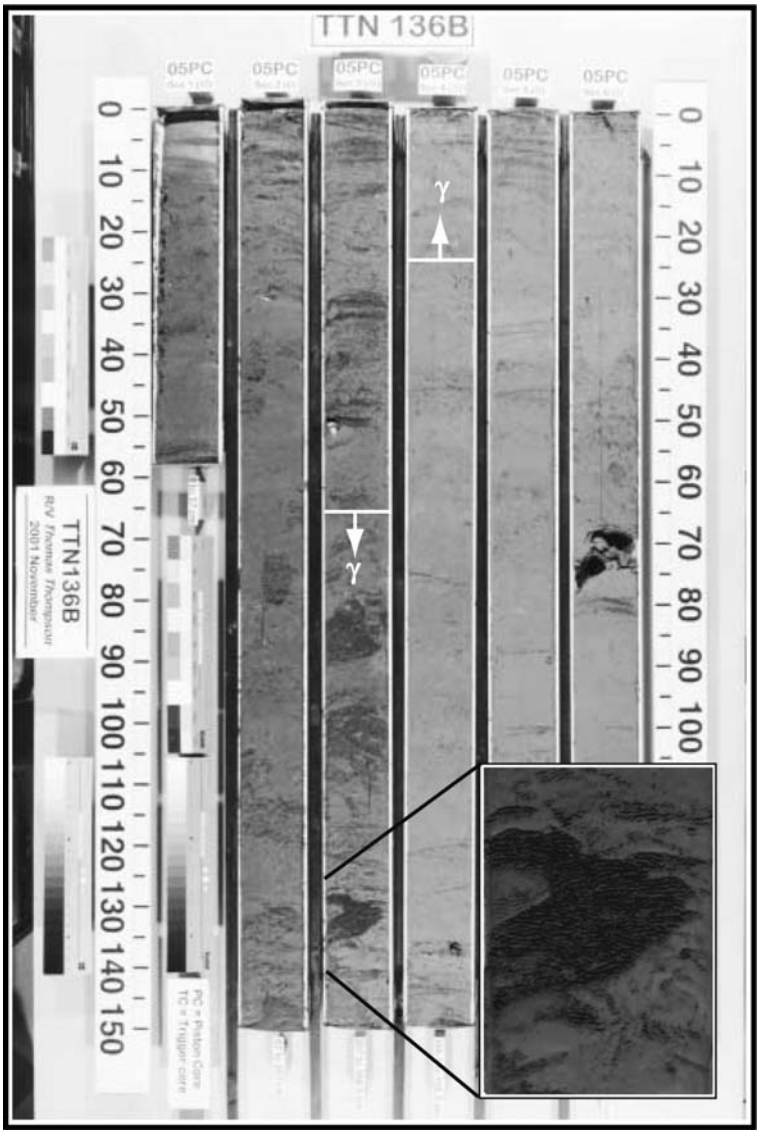

Fig. 16. Core 5 photograph. The inset shows an apparent folded layer within the deformed γ zone.

the origin of these features continues. AMS measurements provide additional constraints on the origin of these features and are discussed below.

5.1. α — *alpha*

The high χ_{lf}, ARM and IRM characteristic of the α zone is different than the other underlying zones observed in the cores. Given that the high ARM and IRM values are only observed in the upper sections of the cores, Figs. 11 and 12 suggest that the base of α is either (1) a diagenetic front delineating the top of the sulphate reduction zone, where biomediation consumes a fraction of the ferro magnetic grains; or (2) a mineralogical change reflecting a change in sediment discharge from the Eel River system. Diagenetic signatures in rock magnetic parameters (e.g. χ_{lf}, ARM, IRM) have been reported by numerous authors from a wide range of environments around the world (e.g. Karlin, 1990b; Leslie et al., 1990b; Tarduno, 1994; Liu et al., 2004; Geiss et al., 2004; Kumar et al., 2005; Pan et al., 2005; Riedinger et al., 2005; Rowan and Roberts, 2006). These transitions are typically attributed to a sulfate reduction in sediments that preferentially consume magnetites with large surface area to volume ratios (e.g., smaller grain size). Karlin (1990b) concluded that magnetic mineral diagenesis is likely to occur in rapidly deposited, sulfidic sediments. The process may shutdown

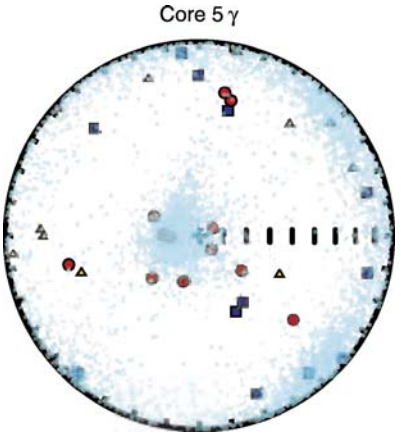

Fig. 17. The γ interval is only observed in Core 5. This zone is located between two β zones. γ has triaxial samples, low χ_{lf}, and V_3 vectors that deviate significantly from vertical.

after the initial reactions, not because of the complete removal of magnetite, but from the magnetites becoming covered in a protective coating of pyrite (Egli, 2004).

The ARM versus χ_{lf} bi-plots show that the α zone is separate from the other zones that have moderate or low ARM and IRM values (Fig. 12). King et al. (1983) reported that for a line passing through the origin and through a group of measurements on an ARM versus χ_{lf} plot (they use χ_{ARM}, which is a normalized form of ARM), the slope of the line is related to the size distribution of the magnetites in the samples. Steeper slopes are indicative of finer grained magnetites, whereas shallower slopes are evidence for coarser grained magnetites. If this relationship holds for the sediments in this study, then the most recently deposited sediments (the tops of the cores, α zone) have a finer grained fraction of magnetites than the underlying zones. These magnetites are consumed in the reaction front and are no longer present in the deeper sediments. This hypothesis implies that the finer grained magnetite population is situated in such a fashion as to generate a triaxial fabric. Below the diagenetic front where the finer-grained magnetites have been consumed, an oblate anisotropy is observed for the individual samples (Figs. 6, 7, and 8). It is difficult to explain why the fine-grained magnetites have such strong anisotropy and thus it is not our preferred hypothesis. Unfortunately, dissolution of the finer grained fraction makes no prediction of the source of this easily reduced magnetite.

The second hypothesis is that á correlates with a shift in sediment provenance. There is a higher weight percent fraction of 63–300 μm grains in the α zone with respect to the underlying zones (Fig. 11). The Eel River area is undergoing a number of changes that could have caused such a shift. The shift may correlate with the 1955 transition to an increase in frequency of large floods on the Eel River and the widening of the Eel River channel observed by Sloan et al. (2001) and Sommerfield et al. (2002). High flow conditions can cause sediments deposited to have triaxial fabrics (e.g. Kopf and Berhman, 1997), which may explain the triaxial samples in α. If the density flows associated with these floods exhibit different flow directions through the Humboldt slide amphitheater, then they might produce the signature observed in Fig. 10 where the triaxial samples girdle the horizontal plane giving an overall group signature of oblate sediment fabric.

In rapidly depositing sediments, it is possible that the rate of deposition and sediment composition control the location of a diagenetic front. Therefore, we can not rule out the possibility that the local shift in the Eel River sediment delivery system may play a role in governing the location of the transition from high to low χ_{lf}, ARM, and IRM.

The results for the α zone show conflicting model interpretations based on that presented in Fig. 3 and are difficult to interpret. The α zone bootstrap inclinations (Table 3: $\bar{I}$) range from 83.1° to 88.1°. This tight vertical V_3 implies quiet water deposition as illustrated in Figs. 3a. Cores 2 and 5 show the strongest evidence for flow directions of 306° and 180° respectively based on V_3 $\bar{D}$ (Table 3).

On the other hand, with the majority of samples being triaxial, one might be tempted to classify the sediments as deformed based on the triaxial histogram shown in Fig. 3c. It is important to distinguish the difference between sample level anisotropy (Figs. 6–9) and group level anisotropy (Fig. 3: bootstrapped eigenvalues). A group level bootstrap histogram tests for coherent deformation, whereas sample level anisotropy test for the statistical distinguishability of the eigenvectors for one specimen. A triaxial sample can imply a number of sediment histories including deformation or deposition under moderate flow conditions. Based on the observations, we interpret alpha to be indicative of deposition in moderate flow conditions.

5.2. β' — *beta prime*

The β' zone is only observed in cores 2 and 5 and is characterized by V_3 deviating from vertical. β' has relatively stable χ_{lf}, ARM, and IRM. The individual samples are predominantly triaxial, but there are several samples that are prolate. Nevertheless, the V_1 orientation shows no preferred direction in the bootstrap. We interpret this to be moderate to strong flow conditions and core 2 may be on the apex of the feature which may have exposed this location to slightly greater currents and/or erosion. Conversely in core 5, the V_3 does not

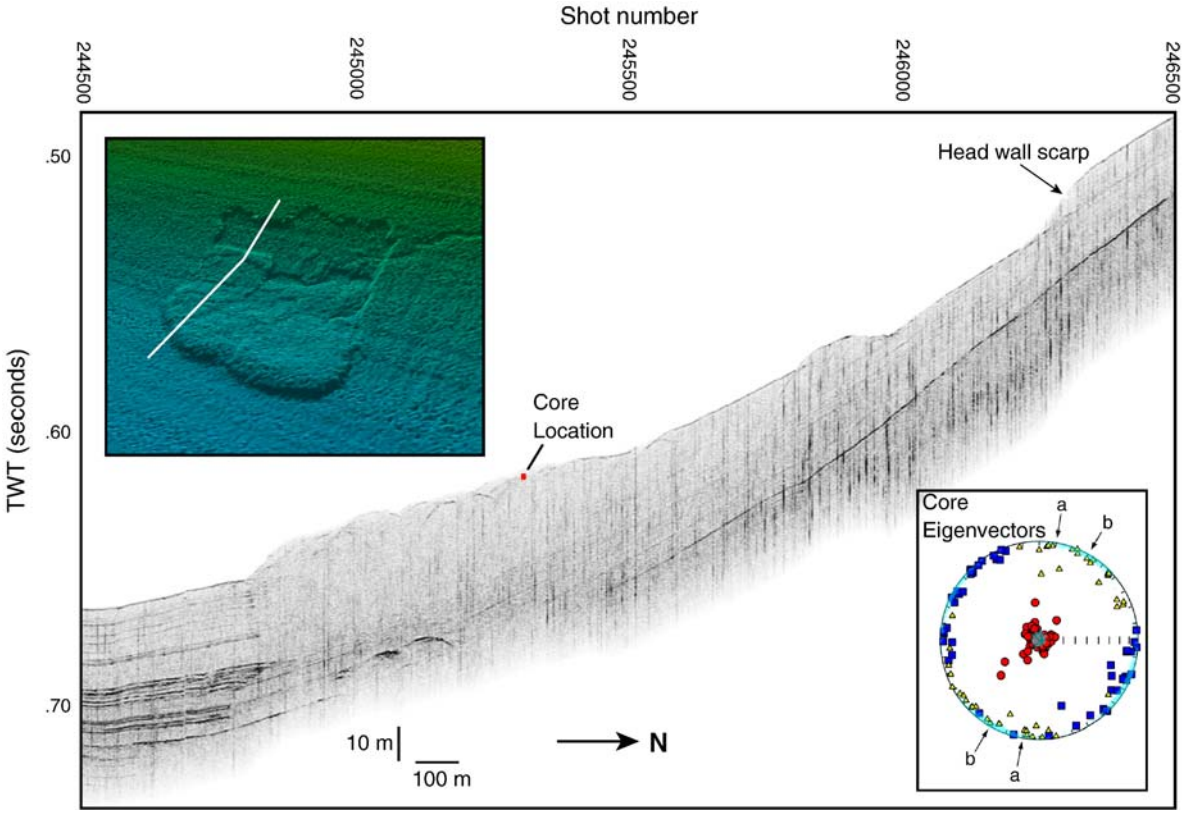

Fig. 18. A CHIRP seismic profile images the Gaviota Slide in the Santa Barbara Basin, southern California (Schwehr et al., in press). Note the clearly defined head scarp and thickening in the accumulation zone at the base of the slide. The inset shows the slide in EM300 from MBARI (Eichhubl et al., 2002). The expected direction of compression based on morphology is indicated by arrow (a). The direction of compression from the eigenvectors, shown by arrow (b), closely matches.

exhibit as much deflection, which may be indicative of more moderate flow. Core 2 sampled high flow conditions that appear to be centered on 325° (Table 3), which would be consistent with predicted flow directions. The observation that cores 1 and 7 do not exhibit β' zones implies that the β' zone observed in core 2 is a local feature with little lateral extent.

5.3. β — *beta*

The marked shift to more oblate sample and group shape fabric defines the β zone, which implies quiet water deposition. This conclusion is a bit surprising considering the size and frequency of large organic-rich layers within the zone (e.g. Fig. 8: β and 15). This may be caused by how flows attach to and detach from the bottom as they travel over an undulating sea floor.

This is the zone where the best evidence should be found for the deformation predicted by the slope failure model (Gardner et al., 1999). The geometry observed in CHIRP and Huntec seismic data (Figs. 4 and 5) predict thickening of 2:1 or greater on the upslope limbs. This amount of compression is expected to create fabric like that illustrated in Fig. 3c. However, the eigenvectors plotted on stereonets with bootstrap eigenvectors for β most closely resemble Fig. 3a. Core 7 is the least like Fig. 3a, but the bootstrap eigenvectors are tightly clustered near vertical. The scatter in the eigenvectors can be traced to samples in four discrete regions located at ~ 167, 261–282, 420–430, and 572 cm. These layers with V_3 deflected from the vertical might correspond to periods of higher flow. Because the V_1 eigenvalues shows no preferred orientation for β in Core 7, it does not appear to be recording post-depositional deformation.

5.4. γ — *gamma*

γ stands out as the largest region of deflected V_3. The I_{V_3} has a saw-toothed pattern indicating deformation that may not be coherent. This observation is supported by visual inspection of the core photograph, which shows a folded organic-rich layer (Fig. 16). Given the degree of

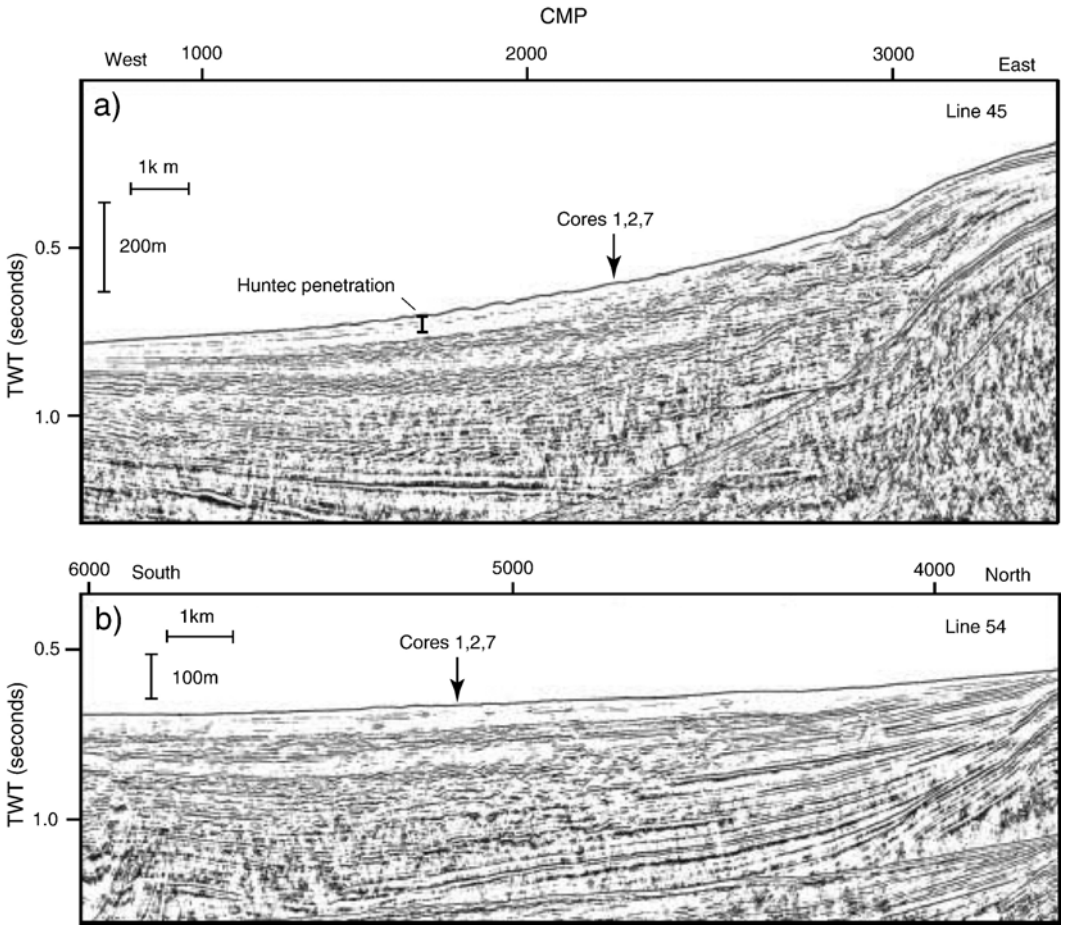

Fig. 19. Cruise W9605B multi-channel seismic lines. Line 45 is a dip line imaging the internal structure of the Humboldt Slide. Line 54 is a strike line across the region that includes the Little Salmon Anticline on the northern side. The location of cores 1, 2, and 7 is marked with an arrow. Line 45 runs from CMP 770 to 3323 that spans 16.0 km. Line 54 is 14.6 km long, from CMP 3698 to 6017.

deformation in γ, it is difficult to assess the direction of compression for this slump. The bootstrap $\bar{D}$ for V_1 is 330°, but this value has an associated ζ of 90°, meaning that $\bar{D}$ for V_1 is not significant. However, the lack of preferred orientation of V_1 in the bootstrap test is consistent with highly deformed and folded sediment (e.g., recumbent folding). Such a deformation pattern exhibits fabrics in the AMS that are similar to deposition under moderate to high flow conditions. Note that γ looks very different from the eigenvectors from the Gaviota Slide shown in Fig. 18 and much more like β' in core 2. Nevertheless, visual examination of the core indicates that the fabric is associated with folding and deformation (Fig. 16).

5.5. The Humboldt Slide as a sediment wave field

We interpret the magnetic and sedimentological data presented here to indicate that there is little to no post-depositional deformation in the Humboldt Slide region. On the basis of the AMS data, we have identified four types of sediment. There is evidence for moderate to strong flow events and small crypto-slump events (usually occurring as a number of events in a restricted region). These crypto-slump events may represent periods of rapid sea level change, high sediment accumulation rates and loading, or increased seismic activity, but currently there is insufficient evidence to test these hypotheses.

The rill area to the north of the Humboldt Slide shows greater evidence for deformation in comparison to the material in the Humboldt Slide amphitheater. The overlying several meter sediment package may be creeping over the underlying sediments.

We observe no evacuation zone or downslope thickening toward the toe of the slide. The units observed in the MCS data (Fig. 19a; described in Burger et al., 2003) thin seaward down the slide. Individual layers exhibit

divergence and thickening towards the margin that may reflect long-term tectonic control in the region (Fig. 19b). The stratal geometry imaged in the MCS data is not consistent with the geometry predicted by the retrogressive failure model.

There is a geometric problem with this feature being interpreted as a slide deposit as it exhibits no thinning in the evacuation zone and no thickening in the accumulation zone. This implies that all deformation is accommodated by in-situ rotation and thickening of beds, with little to no translation. We are unable to identify any signature of such processes beyond occasional thin layers that appear to be deposited in moderate to high flow conditions. The orientation of the V_1 eigenvalues is not suggestive of post-depositional deformation as observed in the Gaviota Slide region (Fig. 18).

These observations support the hypothesis that these features are sediment waves with preferential deposition on the upslope limbs. The sediment waves are composed of both hemipelagic deposits and event beds. Near the base of core 1, 2, and 7, (Figs. 7–9) there is an increase in frequency and thickness of layered units down core. Wood and plant material occurs more frequently down core with some layers being >20 cm thick. This suggests a change in the style and/or type of flood deposits as compared to the present.

6. Conclusions

The main results of our rock magnetic and seismic reflection study are summarized as follows:

(1) The upper ~ 8 m of the Humboldt Slide sediments are not undergoing post-depositional deformation and folding.
(2) The upper section sampled in this study appears to be the result of primary deposition, and thus, we interpret the features to be downslope current-controlled bedforms.
(3) Based on MCS data, the thickness and dip of the subsurface sequences are not consistent with the features being a slide deposit. The sediment structures within the Humboldt Slide appear to be sediment waves that may mantle an older slide.
(4) We identified a ~ 1 m thick slump layer located to the north of the Little Salmon Anticline in the region with extensive rills.
(5) The change in how much and what fraction of material is delivered to the Humboldt Slide area (versus that north of the Little Salmon Anticline and down the Eel Canyon to the south) may have undergone a recent shift caused by the increasing frequency of combined large storm and flood events from 1955 to the present. This possibility requires further research.

Magnetic measurements allow us to test between the alternative hypotheses of slope failure, and sediment waves for the origin of the Humboldt Slide. Specifically, we are able to discern whether the morphology and internal geometry results from soft sediment deformation and retrogressive slumping, or downslope current-controlled deposition. The former predicts a triaxial AMS fabric with essentially north-south oriented maximum axes (Fig. 3c); the latter predicts an oblate fabric with a possible westward deflection of the minimum axes (Fig. 3a,b).

The morphology and internal architecture of the Humboldt Slide are not unique; there are numerous examples along other continental margins with similar morphology and ongoing debates regarding their origin (see examples in Lee et al., 2002). Magnetic methods for the detection of post-depositional deformation provides a new approach to determine the origin of such features on other continental margins.

Acknowledgments

We would like to thank NSF (grant OCE-04-25919), ONR (grant N00014-03-1-0272), and CalIT^2 for funding this research. Additionally we appreciate the support of the crew of the *R/V Thompson*, the OSU Coring Group, the Nittrouer lab and the SIO Geologic Collections. J. Borgeld and his students from Humboldt State University helped out with the cruise. H. J. Lee and J. Gardner provided numerous comments and discussions. J. Gardner provided support in processing the Huntec seismic data. The MCS images (IDs: 4213 and 4226) were acquired from http://www.ig.utexas.edu/sdc/cruise.php?cruiseIn=w9605b, courtesy of C. Fulthorpe and G. Mountain.

References

Alexander, C.R., Simoneau, A.M., 1999. Spacial variability in sedimentary processes on the eel continental slope. Mar. Geol. 154 (1–4), 243–254.

Banerjee, S.K., King, J., Marvin, J., 1981. A rapid method for magnetic granulometry with applications to environmental studies. Geophys. Res. Lett. 8, 333–336.

Booth, J., O'leary, D., Popenoe, P., Danforth, W., 1993. U.S. Atlantic continental slope landslides: their distribution, general attributes, and implications. U.S. Geol. Surv. Bull. 14–22.

Brooks, T., Johnson, K., 1997. Final report, phase 3 and phase 4 seismic program, Owens Lake, Inyo Country, California, vol. 146.

Burger, R.L., Fulthorpe, C.S., Austin Jr., J.A., 2003. Effects of triple junction migration and glacioeustatic cyclicity on evolution of upper slope morphologies, offshore Eel River Basin, Northern California. Mar. Geol. 199 (3–4), 307–336.

Clarke, S.J., 1987. Geology of the California continental margin north of Cape Mendocino. In: Scholl, D., Grantz, A., Vedder, J. (Eds.), Geology and resources potential of the continental margin of western North America and adjacent ocean basins — Beufort Sea to Baja California. Earth Science Series. Circum-Pacific Council for Energy and Mineral Resources, vol. 6, pp. 337–351.

Constable, C., Tauxe, L., 1990. The bootstrap for magnetic susceptibility tensors. J. Geophys. Res. 95, 8383–8395.

Couch, R., 1980. Seismicity and crustal structure near the north end of the San Andreas fault system. In: Streitz, R., Sherbourne, R. (Eds.), Studies of the San Andreas Fault Zone in northern California. Special Reports. Calif. Div. Mines Geol., vol. 190, pp. 13–30.

Cronin, M., Tauxe, L., Constable, C., Selkin, P., Pick, T., 2001. Noise in the quiet zone. Earth Planet. Sci. Lett. 190 (1–2), 13–30.

Dillon, W., Lee, M., Fehlhaber, K., Coleman, D., 1993. Gas hydrates on the Atlantic continental margin of the United States — controls on concentration. In: Howell, D. (Ed.), The future of energy gasses. US Geological Survey Professional Paper, vol. 1570, pp. 313–330.

Dodds, D.J., 1980. Attenuation estimates from high resolution subbottom profiler echoes. Saclant Asw Research Conference on Ocean Acoustics Influenced by the Sea floor, vol. 907. Plenum Press, La Spezia, Italy, p. 19.

Driscoll, N., Diebold, J., 1999. Tectonic and stratigraphic development of the Caribbean: new constraints from multichannel seismic data. In: Mann, P. (Ed.), Caribbean Basins. Sedimentary Basins of the World, vol. 4. Elsevier Science B.V., Amsterdam, pp. 591–627.

Driscoll, N.W., Hogg, J.R., 1995. Stratigraphic response to basin formation: Jeanne d'arc basin, off shore Newfoundland. Geol. Soc. Spec. Publ. 80 (Hydrocarbon Habitat in Rift Basins).

Egli, R., 2004. Characterization of individual rock magnetic components by analysis of remanence curves. 3. Bacterial magnetite and natural processes in lakes. Phys. Chem. Earth 29 (13–14), 869–884.

Eichhubl, P., Greene, H.G., Maher, N., 2002. Physiography of an active transpressive margin basin: high-resolution bathymetry of the Santa Barbara Basin, Southern California continental borderland. Mar. Geol. 184 (1–2), 95–120.

Embley, R., Jacobi, R., 1986. Mass wasting in the western North Atlantic. In: Vogt, P., Tucholke, B. (Eds.), The Western North Atlantic region. Vol. M. Boulder Colorado. Geological Society of America, pp. 479–490.

Evans, D., King, E., Kenyon, N., Brett, C., Wallis, D., 1996. Evidence for long-term instability in the Storegga Slide region off western Norway. Mar. Geol. 130, 281–292.

Field, M., Barber, J., 1993. A submarine landslide associated with shallow sea-floor gas and gas hydrates off northern California. In: Schwab, W., Lee, H., Twitchell, D. (Eds.), Submarine Landslides: Selected Studies in the U.S. Exclusive Economic Zone. Unites States Geological Survey Bulletin, vol. 2002.

Fisher, R.A., 1953. Dispersion on a sphere. Proc. R. Soc. London, Ser. A 217, 295–305.

Galway, R.S., 2000. The integration of multibeam sonar data with Huntec sub-bottom profile data into a marine GIS. Masters of Science in Engineering. University of New Brunswick.

Gardner, J., Prior, D., Field, M., 1999. Humboldt Slide — a large shear-dominated retrogressive slope failure. Mar. Geol. 154, 323–338.

Geiss, C.E., Banerjee, S.K., Camill, P., Umbanhowar, C.E., 2004. Sediment-magnetic signature of land-use and drought as recorded in lake sediment from south-central Minnesota, USA. Quat. Res. 62 (2), 117–125.

Glen, J., Coe, R., 1997. Paleomagnetism and magnetic susceptibility of Pleistocene sediments from drill hole OL-92, Owens Lake, California. In: Smith, G., Bischoff, J. (Eds.), An 800,000-year Geologic and Climatic record from Owens Lake, California: Core OL-92. Geological Society of America, pp. 67–78.

Gutowski, M., Bull, J.M., Henstock, T., Dix, J.K., Hogarth, P., Leighton, T., White, P., 2002. Chirp sub-bottom profiler source signature design and field testing. Mar. Geophys. Res. 23 (5–6), 481–492.

Henkart, P., 2006. Siosies. http://sioseis.ucsd.edu.

Hext, G.R., 1963. The estimation of second-order tensors, with related tests and designs. Biometrika 50, 353–357.

Holbrook, W., 2001. Seismic studies of the Blake Ridge: implications for hydrate distribution, methane expulsion, and free gas dynamics. In: Paull, C., Dillon, W. (Eds.), Natural Gas Hydrates: Occurrence, Distribution, and Detection. Geophysical Monograph, vol. 124. AGU.

Holbrook, W., Lizarralde, D., Pecher, I., Gorman, A., Hackwith, K., Hornbach, M., Saffer, D., 2002. Escape of methane gas through sediment waves in a large methane hydrate province. Geology 30 (5), 467–470.

Housen, B.A., Kanamatsu, T., 2003. Magnetic fabrics from the Costa Rica margin: sediment deformation during the initial dewatering and underplating process. Earth Planet. Sci. Lett. 206 (1–2), 215–228.

Housen, B.A., Richter, C., van der Pluijm, B., 1993. Composite magnetic anisotropy fabrics: experiments, numerical models, and implications for the quantification of rock fabrics. Tectonophysics 220, 1–12.

Housen, B.A., Tobin, H., Labaume, P., Leitch, E., Maltman, A., Shipley, T., Ogawa, Y., Ashi, J., Blum, P., Bruckman, W., Felice, F., Fisher, A., Goldberg, D., Henry, P., Jurado, M., Kastner, M., Laier, T., Meyer, A., Moore, J., Moore, G., Peacock, S., Rabaute, A., Steiger, T., Underwood, M., Xu, Y., Yin, H., Zheng, Y., Zwart, G., 1996. Strain decoupling across the decollement of the Barbados accretionary prism. Geology 24 (2), 127–130.

Hrouda, F., Hruskova, L., 1990. On the detection of weak strain parallel to the bedding by magnetic anisotropy: a mathematical model study. Studia Geophys. Geol. 34, 327–341.

Ising, G., 1942. On the magnetic properties of varved clay. Arkiv. For. Mate., Astr., Och Fys. 29, 1–37.

Kanamatsu, T., Herrero-Bervera, E., Taira, A., 2001. Magnetic fabrics of soft-sediment folded strata within a Neogene accretionary complex, the Miura group, central Japan. Earth Planet. Sci. Lett. 187 (3–4), 333–343.

Karlin, R., 1990a. Magnetic mineral diagenesis in suboxic sediments at Bettis Site W-N, NE Pacific Ocean. J. Geophys. Res. 95 (B4), 4421–4436.

Karlin, R., 1990b. Magnetite diagenesis in marine sediments from the Oregon continental margin. J. Geophys. Res. 95 (B4), 4405–4419.

King, J., Banerjee, S.K., Marvin, J., Ozdemir, O., 1982. A comparison of different magnetic methods for determining the relative grain size of magnetite in natural materials: some results from lake sediments. Earth Planet. Sci. Lett. 59, 44–419.

King, J., Banerjee, S.K., Marvin, J., 1983. A new rock-magnetic approach to selecting sediments for geomagnetic paleointensity studies: application to paleointensity for the last 4000 years. J. Geophys. Res. 88 (B7), 5911–5921.

Kopf, A., Berhman, J.H., 1997. Fabric evolution and mechanisms of diagenesis in fine-grained sediments from the Kita–Yamato Trough, Japan Sea. J. Sediment. Res. 67 (3), 590–600.

Kumar, A.A., Rao, V.P., Patil, S.K., Kessarkar, P.M., Thamban, M., 2005. Rock magnetic records of the sediments of the eastern Arabian sea: evidence for late quaternary climatic change. Mar. Geol. 220 (1–4), 59–82.

Lee, H.J., Syvitski, J.P.M., Parker, G., Orange, D., Locat, J., Hutton, E.W.H., Imran, J., 2002. Distinguishing sediment waves from slope failure deposits: field examples, including the ‘‘Humboldt Slide”, and modelling results. Mar. Geol. 192 (1–3), 79–104.

Leslie, B.W., Hammond, D.E., Berelson, W.M., Lund, S.P., 1990a. Diagenesis in anoxic sediments from the California continental borderland and its influence on iron, sulfur, and magnetite behavior. J. Geophys. Res. 95 (B4), 4453–4470.

Leslie, B.W., Lund, S.P., Hammond, D.E., 1990b. Rock magnetic evidence for the dissolution and authigenic growth of magnetic minerals within anoxic marine sediments of the California continental borderland. J. Geophys. Res. 95 (B4), 4437–4452.

Liu, J., Zhu, R., Roberts, A.P., Li, S., Chang, J.-H., 2004. High-resolution analysis of early diagenetic effects on magnetic minerals in post-middle-Holocene continental shelf sediments from the Korea Strait. J. Geophys. Res. 109 (B03103). doi:10.1029/2003JB002813.

Marino, R., Ellwood, B., 1978. Anomalous magnetic fabric in sediments which record an apparent geomagnetic field excursion. Nature 274, 581–582.

Nittrouer, C., 1999. Strataform: overview of its design and synthesis of its results. Mar. Geol. 154, 3–12.

Owens, W.H., 1974. Mathematical model studies on factors affecting the magnetic anisotropy of deformed rocks. Tectonophysics 24, 115–131.

Pan, Y., Petersen, N., Davila, A.F., Zhang, L., Winklofer, M., Liu, Q., Hanzlik, M., Zhu, R., 2005. The detection of bacterial magnetite in recent sediments of Lake Chiemsee (southern Germany). Earth Planet. Sci. Lett. 232 (1–2), 109–123.

Pares, J., van der Pluijm, B., Dinares-Turell, J., 1999. Evolution of magnetic fabrics during incipient deformation of mudrocks (Pyreness, northern Spain). Tectonophysics 307, 1–14.

Pratson, L.F., Coakley, B.J., 1996. A model for the headward erosion of submarine canyons induced by downslope eroding sediment flows. Geol. Soc. Amer. Bull. 108 (2), 225–234.

Quinn, R., Bull, J.M., Dix, J.K., 1998. Optimal processing of marine high-resolution seismic reflection (chirp) data. Mar. Geophys. Res. 20 (1), 13–20.

Rees, A.I., 1961. The effect of water currents on the magnetic remanence and anisotropy of susceptibility of some sediments. Geophys. J. R. Astron. Soc. 6, 235–251.

Rees, A., 1983. Experiments on the production of transverse grain alignment in a sheared dispersion. Sedimentology 30, 437–448.

Rees, A.I., Woodall, W.A., 1975. The magnetic fabric of some laboratory deposited sediments. Earth Planet. Sci. Lett. 25, 121–130.

Riedinger, N., Pfeifer, K., Kasten, S., Garmin, J.F.L., Vogt, C., Hensen, C., 2005. Diagenetic alteration of magnetic signals by anaerobic oxidation of methane related to a change in sedimentation rate. Geochim. Cosmochim. Acta 69 (16), 4117–4126.

Rosenbaum, J., Reynolds, R., Smoot, J., Meyer, R., 2000. Anisotropy of magnetic susceptibility as a tool for recognizing core deformation: reevaluation of the paleomagnetic record of Pleistocene sediments from drill hole OL-92, Owens Lake, California. Earth Planet. Sci. Lett. 178, 415–424.

Rowan, C.J., Roberts, A.P., 2006. Magnetite dissolution, diachronous greigite formation, and secondary magnetizations from pyrite oxidation: unravelling complex magnetizations in Neogene marine sediments from New Zealand. Earth Planet. Sci. Lett. 241 (1–2), 119–137.

Schock, S.G., LeBlanc, L.R., Panda, S., 1994. Spatial and temporal pulse design considerations for a marine sediment classification sonar. IEEE J. Oceanic Eng. 19 (3), 406–415.

Schwehr, K., Tauxe, L., 2003. Characterization of soft sediment deformation: detection of crypto-slumps using magnetic methods. Geology 31 (3), 203–206.

Schwehr, K., Tauxe, L., Driscoll, N., Lee, H., in press. Detecting compaction disequilibrium with anisotropy of magnetic susceptibility. Geochem., Geophys., Geosyst. 7 (1). doi:10.1029/2006GC001378.

Sloan, J., Miller, J.R., Lancanster, N., 2001. Response and recovery of the Eel River, California, and its tributaries to floods in 1955, 1964, and 1997. Geomorphology 36 (3–4), 129–154.

Sommerfield, C., Drake, D.E., Wheatcroft, R.A., 2002. Shelf record of climatic changes in flood magnitude and frequency, north-coastal California. Geology 30 (5), 395–398.

Spinelli, G., Field, M., 2001. Evolution of continental slope gullies on the northern California margin. J. Sediment. Res. 71 (2), 237–245.

Tarduno, J.A., 1994. Temporal trends of magnetic dissolution in the pelagic realm: gauging paleoproductivity? Earth Planet. Sci. Lett. 123 (1–3), 39–48.

Tarling, D.H., Hrouda, F., 1993. The Magnetic Anisotropy of Rocks. Chapman and Hall, London.

Tauxe, L., 1998. Paleomagnetic Principles and Practice. Klewer Academic Publishers.

Tauxe, L., Bertram, H., Seberino, C., 2002. Physical interpretation of hysteresis loops: micromagnetic modelling of fine particle magnetite. Geochem. Geophys. Geosyst. 3 (10). doi:10.1029/ 2001GC000280.

Trincardi, F., Cattaneo, A., Correggiari, A., Ridente, D., 2004. Evidence of soft sediment deformation, fluid escape, sediment failure and regional weak layers within the late Quaternary mud deposits of the Adriatic Sea. Mar. Geol. 213 (1–4), 91–119.